THE ASTROPHYSICAL JOURNAL, 470:551–565, 1996 October 10

RADIATIVE TORQUES ON INTERSTELLAR GRAINS. I. SUPERTHERMAL SPIN-UP

B. T. DRAINE
Princeton University Observatory, Peyton Hall, Princeton, NJ 08544; draine@astro.princeton.edu
AND
JOSEPH C. WEINGARTNER
Physics Department, Jadwin Hall, Princeton University, Princeton, NJ 08544; josephw@phoenix.princeton.edu
Received 1996 February 12; accepted 1996 May 2

ABSTRACT

Irregular dust grains are subject to radiative torques when irradiated by interstellar starlight. It is shown how these radiative torques may be calculated using the discrete dipole approximation. Calculations are carried out for one irregular grain geometry and three different grain sizes. It is shown that radiative torques can play an important dynamical role in spin-up of interstellar dust grains, resulting in rotation rates that may exceed even those expected from H_2 formation on the grain surface. Because the radiative torque on an interstellar grain is determined by the overall grain geometry rather than merely the condition of the grain surface, the resulting superthermal rotation is expected to be quite long-lived. By itself, long-lived superthermal rotation would permit grain alignment by normal paramagnetic dissipation on the "Davis-Greenstein" timescale τ_{DG}. However, radiative torques arising from anisotropy of the starlight background can act directly to alter the grain alignment on times short compared to τ_{DG}. Radiative torques must therefore play a central role in the process of interstellar grain alignment.

The radiative torques depend strongly on the grain size, measured by a_{eff}, the radius of a sphere of equal volume. In diffuse clouds, radiative torques dominate the torques due to H_2 formation for $a_{eff} = 0.2$ μm grains, but are relatively unimportant for $a_{eff} \leq 0.05$ μm grains. We argue that this may provide a natural explanation for the observation that $a_{eff} \gtrsim 0.1$ μm grains in diffuse clouds are aligned, while there is very little alignment of $a_{eff} \lesssim 0.05$ μm grains. We show that radiative torques are ineffective at producing superthermal rotation within quiescent dark clouds, but can be very effective in star-forming regions such as the M17 molecular cloud.

Subject headings: ISM: dust, extinction — polarization — radiative transfer — scattering

1. INTRODUCTION

Polarization of starlight by aligned interstellar dust grains was discovered nearly half a century ago (Hiltner 1949a, 1949b; Hall 1949; Hall & Mikesell 1949), but the processes responsible for the observed alignment remain uncertain. Davis & Greenstein (1951) observed that interstellar grains were expected to be rotating rapidly as a result of Brownian motion, and proposed that these spinning grains could be aligned with the local magnetic field by paramagnetic dissipation. However, further study of the statistical mechanics of grain alignment (Jones & Spitzer 1967; Purcell & Spitzer 1971) raised questions about the ability of the interstellar magnetic field to achieve the observed degree of alignment, since random gas-grain collisions would tend to oppose the alignment process.

Purcell (1975, 1979) first recognized that interstellar grains were expected to have superthermal rotational velocities as the result of systematic torques, the most important of which appeared to be due to the process of H_2 formation on the grain surface. As discussed by Purcell, superthermal rotation due to torques that are fixed in body coordinates can enhance the degree of grain alignment, since the "thermal" torques due to random collisions with gas atoms now have little effect on the direction of the grain angular momentum, allowing paramagnetic dissipation to inexorably bring the angular momentum into alignment with the galactic field.

The systematic torques considered by Purcell were due to processes taking place at the grain surface—H_2 formation, photoelectric emission, and inelastic collisions with gas atoms—but the grain surface may be altered as a result of contamination or erosion on relatively short timescales. The resulting changes in direction of the systematic torque can cause the grain to occasionally undergo short periods when its rotation is "spun down"; during these "crossover" episodes, the grain may become disaligned (Spitzer & McGlynn 1979). Because of this disorientation during "crossover," it was not clear whether ordinary paramagnetic dissipation plus superthermal rotation driven by "Purcell torques" can account for the observed grain alignment.

In addition, dust grains were observed to be aligned in some dense molecular regions where "Purcell torques" were expected to be ineffective because of a low H/H_2 ratio, attenuation of the ultraviolet radiation required for photoelectric emission, and near-equality of gas and grain temperatures. As a result, there has been renewed interest in alternatives, including the possibility that grains may be superparamagnetic (Jones & Spitzer 1967; Duley 1978; Martin 1995; Goodman & Whittet 1995), or that grain alignment is due to gas-grain streaming (Gold 1952; Lazarian 1994, 1995a; Roberge, Hanany, & Messinger 1995). Lazarian (1995b) has emphasized the possible importance of grain "helicity," since helical grains can be driven to superthermal rotational velocities, and possibly aligned, when exposed to either streaming gas atoms or anisotropic radiation.

Harwit (1970a, 1970b) suggested that the quantized angular momentum of the photon could lead to rapid rotation of a grain following absorption and emission of many photons, and proposed that the anisotropy of starlight

could result in a tendency for interstellar grains to spin with their angular momentum vectors parallel to the Galactic plane. Dolginov (1972) observed that interstellar grains might have different absorption and scattering cross sections for left- and right-handed circularly polarized light, so that the grain angular momentum could be changed if illuminated by unpolarized but anisotropic radiation. This effect was further discussed by Dolginov & Mytrophanov (1976) for particles in the Rayleigh limit, and by Dolginov & Silant'ev (1976) for larger particles but with refractive index close to unity so that the Rayleigh-Gans approximation could be used. Dolginov & Mytrophanov (1976) noted that this process could lead to both rapid rotation and possible alignment. Unfortunately, Dolginov and collaborators were unable to calculate the torques on grains with realistic compositions and sizes.

That irregular interstellar grains should be subject to radiative torques is not surprising. We consider two macroscopic examples for illustration. Figure 1*a* shows a fourfold symmetric target with square top and bottom, with each of its four rectangular sides divided into perfectly absorbing and perfectly reflecting halves. In the geometric optics limit, the normal component of the radiation pressure force will be twice as large on the reflecting sections as on the absorbing sections; as a result, an isotropic radiation field illuminating this target will produce a positive torque along axis $\hat{a}_1$. However, incident radiation that is either parallel or antiparallel to $\hat{a}_1$ will not produce any torque on this target.

Figure 1*b* shows a target obtained by starting with the shape of Figure 1*a* and removing four wedges from the top and four from the bottom, with the resulting shape being symmetric under reflection through the centroid. Figure 1*b* is an example of a shape with "helicity." From symmetry it is clear that an isotropic radiation field will produce no torque on this target: whatever torque is exerted on the "top" half of the grain will be canceled by an opposite torque on the "bottom" half. However, anisotropic illumination can produce a torque on this target. If, for example, the surfaces are all perfectly reflecting, then incident radiation that is antiparallel to $\hat{a}_1$ will produce a torque parallel to $\hat{a}_1$, while radiation parallel to $\hat{a}_1$ will produce a torque antiparallel to $\hat{a}_1$. These two examples show that macroscopic objects will be subject to radiative torques unless they are highly symmetric; thus, irregular targets should generally be subject to radiative torques. Interstellar grains are, of course, comparable to or smaller than the wavelength of the illuminating radiation, but one does not expect the radiative torques to vanish when target geometries

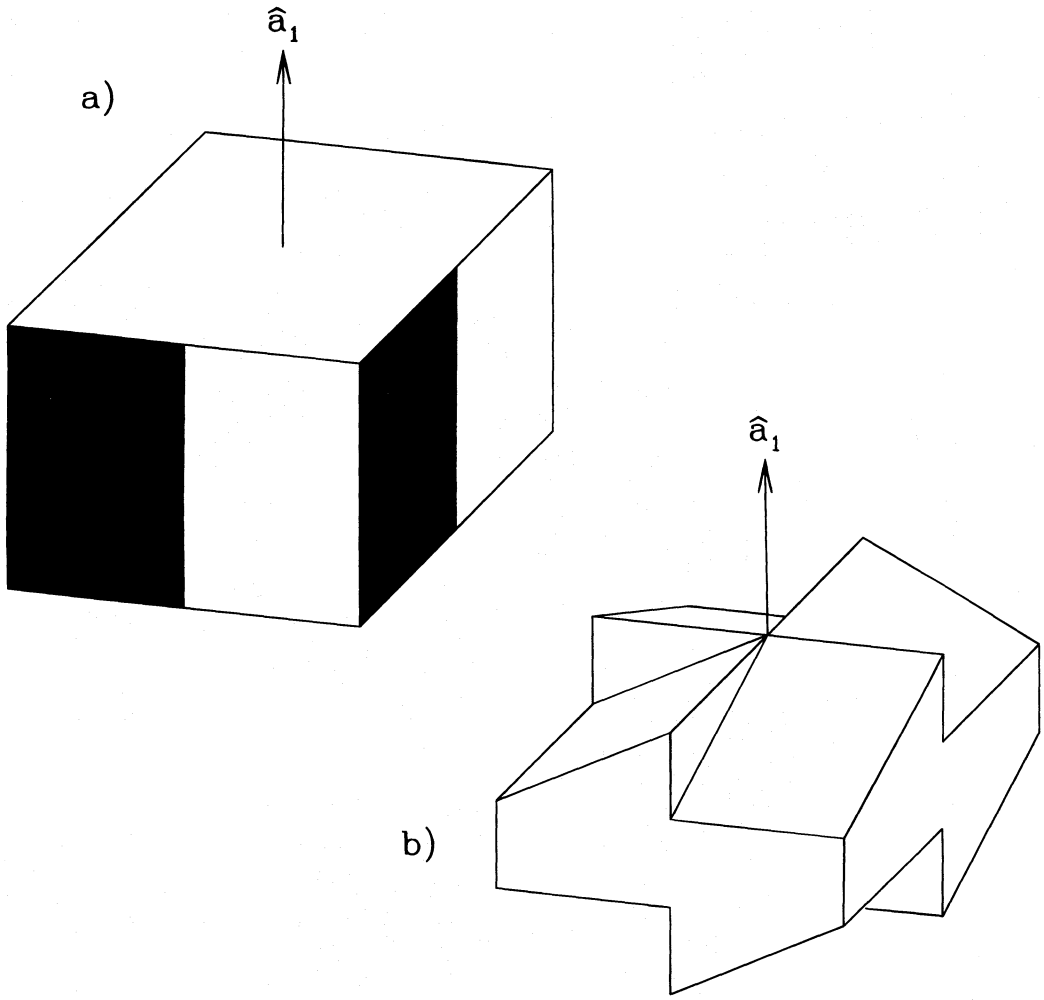

FIG. 1.—Two examples of macroscopic targets. (*a*) A target on which an isotropic radiation field would exert a torque along axis $\hat{a}_1$. The target is perfectly reflecting except for the regions painted black. (*b*) A perfectly reflecting target on which an isotropic radiation field would exert zero torque: radiation antiparallel to $\hat{a}_1$ would exert a positive torque parallel to $\hat{a}_1$, and radiation parallel to $\hat{a}_1$ would exert a torque antiparallel to $\hat{a}_1$.

such as in Figure 1 are reduced to sizes comparable to the wavelength.

In this paper we discuss the forces and torques on grains of arbitrary shape and with sizes that are neither large nor small compared to the wavelength of the incident radiation. We show how these forces and torques can be calculated using the discrete dipole approximation. Quantitative results are obtained for one particular irregular grain shape.

The first part of this paper, §§ 2–5, is devoted to development of the theory of scattering by irregular particles to enable efficient computation of radiative torques. This is carried out within the conceptual (and computational) framework of the discrete dipole approximation. In § 6 we report results of extensive computations for one specific irregular grain geometry and composition, and three different sizes, $a_{\rm eff} = 0.2$, 0.05, and 0.02 μm ($a_{\rm eff}$ is the radius of a sphere of equal volume).

Readers primarily interested in the implications for grain rotation may elect to skip §§ 2–6, and proceed directly to § 7, where we discuss the effects of starlight and gas drag under realistic conditions in interstellar diffuse clouds, and § 8, where the resulting superthermal rotation is evaluated. It is seen in § 8.3 that moderately anisotropic starlight can torque $a_{\rm eff} = 0.2$ μm grains in diffuse clouds up to extremely large rotational velocities, exceeding even the superthermal rotation due to H_2 formation. Smaller ($a_{\rm eff} \lesssim 0.05$ μm) grains, on the other hand, are only weakly affected by radiative torques.

We also examine the importance of radiative torques within quiescent dark clouds (§ 8.4), and within active star-forming regions (§ 8.5).

Our results are summarized in § 9. Our principal result is that the torques exerted on interstellar grains by background starlight are dynamically very important for grains with $a_{\rm eff} \gtrsim 0.1$ μm. These torques will produce extreme superthermal rotation of interstellar grains in both diffuse clouds and star-forming clouds. In a separate paper (Draine & Weingartner 1996) we examine the role of these radiative torques in the alignment of interstellar grains with the Galactic magnetic field.

2. THE DISCRETE DIPOLE APPROXIMATION

We adopt the "discrete dipole approximation" (Draine & Flatau 1994), and represent the target by an array of polarizable points, at locations $\boldsymbol{r}_j$, with electric polarizabilities α_j. The space between the points is vacuum. We consider the response of this array to monochromatic illumination, and adopt the usual complex representation for all time-dependent variables that are first-order (i.e., $\boldsymbol{E}$ and $\boldsymbol{B}$ fields, and dipole moments $\boldsymbol{p}_j$). Second-order variables (i.e., forces $\boldsymbol{F}$ and torques $\boldsymbol{\Gamma}$) will be taken to be purely real. We assume an incident plane wave

$$\boldsymbol{E}_{\rm inc} = \boldsymbol{E}_{\rm inc,0} \exp\left(i\boldsymbol{k}\cdot\boldsymbol{r} - i\omega_0 t\right), \tag{1}$$

$$\boldsymbol{B}_{\rm inc} = \boldsymbol{B}_{\rm inc,0} \exp\left(i\boldsymbol{k}\cdot\boldsymbol{r} - i\omega_0 t\right), \tag{2}$$

$$\boldsymbol{B}_{\rm inc,0} = \hat{\boldsymbol{k}} \times \boldsymbol{E}_{\rm inc,0}, \tag{3}$$

where the unit vector $\hat{\boldsymbol{k}} \equiv \boldsymbol{k}/k$, and $k = \omega_0/c$. By suitable choice of complex $\boldsymbol{E}_{\rm inc,0}$, we can represent general elliptical polarization.

The dipole at location $\boldsymbol{r}_j$ acquires a dipole moment

$$\boldsymbol{p}_j(t) = \boldsymbol{p}_j(0)e^{-i\omega_0 t} = \alpha_j \boldsymbol{E}_j, \tag{4}$$

where $\boldsymbol{E}_j$ is the electric field at $\boldsymbol{r}_j$ due to the incident electromagnetic field and all dipoles except dipole j:

$$\boldsymbol{E}_j = \boldsymbol{E}_{{\rm inc},j} + \boldsymbol{E}_{{\rm sca},j}, \tag{5}$$

$$\boldsymbol{E}_{{\rm inc},j} = \boldsymbol{E}_{\rm inc,0} \exp\left(i\boldsymbol{k}\cdot\boldsymbol{r}_j - i\omega_0 t\right), \tag{6}$$

$$\boldsymbol{E}_{{\rm sca},j} = e^{-i\omega_0 t}\sum_{l\neq j}\frac{e^{ikr_{jl}}}{r_{jl}^3}\left\{k^2\boldsymbol{r}_{jl}\times(\boldsymbol{p}_l\times\boldsymbol{r}_{jl}) + \frac{(1-ikr_{jl})}{r_{jl}^2}\left[3\boldsymbol{r}_{jl}(\boldsymbol{r}_{jl}\cdot\boldsymbol{p}_l) - r_{jl}^2\boldsymbol{p}_l\right]\right\}, \tag{7}$$

where $\boldsymbol{r}_{jl} \equiv \boldsymbol{r}_j - \boldsymbol{r}_l$. Similarly, the magnetic field at $\boldsymbol{r}_j$ may be written

$$\boldsymbol{B}_j = \boldsymbol{B}_{{\rm inc},j} + \boldsymbol{B}_{{\rm sca},j}, \tag{8}$$

$$\boldsymbol{B}_{{\rm inc},j} = \boldsymbol{B}_{\rm inc,0} \exp\left(i\boldsymbol{k}\cdot\boldsymbol{r}_j - i\omega_0 t\right), \tag{9}$$

$$\boldsymbol{B}_{{\rm sca},j} = e^{-i\omega_0 t}\sum_{l\neq j} k^2\frac{e^{ikr_{jl}}}{r_{jl}^2}(\boldsymbol{r}_{jl}\times\boldsymbol{p}_l)\left(1-\frac{1}{ikr_{jl}}\right), \tag{10}$$

(see, e.g., Jackson 1975).

3. ELECTROMAGNETIC FORCE ON A GRAIN

The instantaneous force on point dipole j is

$$\boldsymbol{F}_j = \left[\mathrm{Re}\left(\boldsymbol{p}_j\cdot\nabla_j\right)\mathrm{Re}\left(\boldsymbol{E}_j\right) + \frac{1}{c}\mathrm{Re}\left(\frac{d\boldsymbol{p}_j}{dt}\right)\times\mathrm{Re}\left(\boldsymbol{B}_j\right)\right]. \tag{11}$$

The first term in equation (11) is due to gradients in the local electric field; the second is the Lorentz force on the currents associated with the oscillating dipole moments.

It is convenient to separate the total force $\boldsymbol{F}_{\rm rad} = \sum_j \boldsymbol{F}_j$ into two terms:

$$\boldsymbol{F}_{\rm rad} = \boldsymbol{F}_{\rm inc} + \boldsymbol{F}_{\rm sca}, \tag{12}$$

where

$$\boldsymbol{F}_{\rm inc} = \sum_{j=1}^{N}\left[\mathrm{Re}\left(\boldsymbol{p}_j\cdot\nabla_j\right)\mathrm{Re}\left(\boldsymbol{E}_{{\rm inc},j}\right) + \frac{1}{c}\mathrm{Re}\left(\frac{d\boldsymbol{p}_j}{dt}\right)\times\mathrm{Re}\left(\boldsymbol{B}_{{\rm inc},j}\right)\right], \tag{13}$$

$$\boldsymbol{F}_{\rm sca} = \sum_{j=1}^{N}\left[\mathrm{Re}\left(\boldsymbol{p}_j\cdot\nabla_j\right)\mathrm{Re}\left(\boldsymbol{E}_{{\rm sca},j}\right) + \frac{1}{c}\mathrm{Re}\left(\frac{d\boldsymbol{p}_j}{dt}\right)\times\mathrm{Re}\left(\boldsymbol{B}_{{\rm sca},j}\right)\right]. \tag{14}$$

The time-averaged force is

$$\langle\boldsymbol{F}_{\rm rad}\rangle = \langle\boldsymbol{F}_{\rm inc}\rangle + \langle\boldsymbol{F}_{\rm sca}\rangle. \tag{15}$$

Letting x^* denote the complex conjugate of x, it is straightforward to show that

$$\langle\boldsymbol{F}_{\rm inc}\rangle = \frac{1}{2}\mathrm{Re}\left\{\sum_{j=1}^{N} ik[\boldsymbol{p}_j^*(0)\cdot\boldsymbol{E}_{\rm inc,0}]\exp\left(i\boldsymbol{k}\cdot\boldsymbol{r}_j\right)\right\} \tag{16}$$

$$= \frac{1}{8\pi}C_{\rm ext}|\boldsymbol{E}_{\rm inc,0}|^2\hat{\boldsymbol{k}}, \tag{17}$$

where $C_{\rm ext}$ is the total extinction cross section, evaluated using the optical theorem (Draine 1988). Thus, $\langle\boldsymbol{F}_{\rm inc}\rangle$ is just

the average rate at which momentum is removed from the incident radiation field.

Direct evaluation of $\langle \boldsymbol{F}_{\rm sca} \rangle$ from equation (14), using equations (7) and (10), involves summing over $N(N-1)$ terms, which for $N \gtrsim 10^3$ becomes computationally prohibitive.[1] Alternatively, we may evaluate the net rate of momentum transport to infinity by the scattered radiation field; let this be denoted $\langle \boldsymbol{F}_{\rm out} \rangle$. Overall momentum conservation requires that the momentum removed from the incident beam either be transferred to the grain or carried off by the outgoing scattered radiation:

$$\frac{1}{8\pi} C_{\rm ext} |\boldsymbol{E}_{\rm inc,0}|^2 \hat{\boldsymbol{k}} = \langle \boldsymbol{F}_{\rm rad} \rangle + \langle \boldsymbol{F}_{\rm out} \rangle \,. \tag{18}$$

Thus, we see that $\langle \boldsymbol{F}_{\rm out} \rangle = -\langle \boldsymbol{F}_{\rm sca} \rangle$: $\boldsymbol{F}_{\rm sca}$ can be thought of as simply the "recoil" of the grain due to the scattered radiation.

The time-averaged rate of transport of momentum by the scattered radiation is

$$\langle \boldsymbol{F}_{\rm out} \rangle = \int r^2 \, d\Omega \, \frac{1}{8\pi} \, {\rm Re} \, (\boldsymbol{E}^*_{\rm rad} \times \boldsymbol{B}_{\rm rad}) \tag{19}$$

$$= \frac{k^4}{8\pi} \int d\Omega \, \hat{\boldsymbol{n}} \left| \sum_{j=1}^{N} \{ \boldsymbol{p}_j(0) - \hat{\boldsymbol{n}}[\hat{\boldsymbol{n}} \cdot \boldsymbol{p}_j(0)] \} e^{-ik\hat{\boldsymbol{n}} \cdot \boldsymbol{r}_j} \right|^2 , \tag{20}$$

where in equation (20) we have assumed the surface of integration to have radius $r \gg \lambda \equiv 2\pi/k$, retaining only the leading terms of $O(r^{-1})$ in $\boldsymbol{E}$ and $\boldsymbol{B}$ (see Appendix A). Each scattering direction requires evaluation of $O(N)$ terms; the angular integrations typically require a few hundred scattering directions for accurate evaluation.

We define a dimensionless radiation pressure efficiency vector $\boldsymbol{Q}_{\rm pr}$ such that the radiation pressure force

$$\langle \boldsymbol{F}_{\rm rad} \rangle = \boldsymbol{Q}_{\rm pr} \, \pi a_{\rm eff}^2 \, \frac{|\boldsymbol{E}_{\rm inc,0}|^2}{8\pi} \,, \tag{21}$$

where the effective target radius $a_{\rm eff} \equiv (3V/4\pi)^{1/3}$, where V is the volume of target material. The vector $\boldsymbol{Q}_{\rm pr}$ depends on both the orientation of the grain and the direction of propagation and polarization of the incident radiation (e.g., linearly or circularly polarized). It is clear that $\boldsymbol{Q}_{\rm pr} \cdot \hat{\boldsymbol{k}}$ is just the quantity usually described as the "radiation pressure efficiency factor" $= Q_{\rm abs} + (1 - \langle \cos\theta \rangle) Q_{\rm sca}$, where $Q_{\rm abs}$ and $Q_{\rm sca}$ are the usual absorption and scattering efficiency factors, and $\langle \cos\theta \rangle$ is the mean value of $\cos\theta$ for the scattered radiation, where θ is the scattering angle (see, e.g., Bohren & Huffman 1983). It is obvious that $\boldsymbol{Q}_{\rm pr} \parallel \hat{\boldsymbol{k}}$ for targets—e.g., spheres—that are symmetric under rotation around an axis parallel to $\hat{\boldsymbol{k}}$.

4. ELECTROMAGNETIC TORQUE ON A GRAIN

We choose a coordinate system such that the grain center-of-mass is at $\boldsymbol{r} = 0$. The instantaneous radiative torque on the grain is

$$\boldsymbol{\Gamma}_{\rm rad} = \sum_{j=1}^{N} \boldsymbol{r}_j \times \boldsymbol{F}_j + \sum_{j=1}^{N} {\rm Re} \, (\boldsymbol{p}_j) \times {\rm Re} \, (\boldsymbol{E}_j) \,. \tag{22}$$

[1] These sums could presumably be evaluated in $O(N \ln N)$ operations using FFT techniques similar to those used for evaluation of the fields $\boldsymbol{E}_j$ (Goodman, Draine, & Flatau 1991), but this has not been implemented here.

As for the force calculation, we separate the radiative torque into "incident" and "scattered" components:

$$\boldsymbol{\Gamma}_{\rm rad} = \boldsymbol{\Gamma}_{\rm inc} + \boldsymbol{\Gamma}_{\rm sca} \,; \tag{23}$$

$\boldsymbol{\Gamma}_{\rm inc}$ is the torque exerted on the oscillating dipoles by $\boldsymbol{E}_{\rm inc}$ and $\boldsymbol{B}_{\rm inc}$, and $\boldsymbol{\Gamma}_{\rm sca}$ is the torque exerted on the oscillating dipoles by the scattered radiation field—i.e., the fields $\boldsymbol{E}_{\rm sca}$ and $\boldsymbol{B}_{\rm sca}$ due to the oscillating dipoles. The time-averaged value of $\boldsymbol{\Gamma}_{\rm inc}$ is straightforward:

$$\langle \boldsymbol{\Gamma}_{\rm inc} \rangle = \frac{1}{2} \, {\rm Re} \left\{ \sum_{j=1}^{N} \boldsymbol{p}_j^*(0) \times \boldsymbol{E}_{\rm inc,0} \, e^{i\boldsymbol{k} \cdot \boldsymbol{r}_j} - i\boldsymbol{k} \times \sum_{j=1}^{N} \boldsymbol{r}_j [\boldsymbol{p}_j^*(0) \cdot \boldsymbol{E}_{\rm inc,0}] e^{i\boldsymbol{k} \cdot \boldsymbol{r}_j} \right\} . \tag{24}$$

As was the case for $\boldsymbol{F}_{\rm sca}$, direct evaluation of $\boldsymbol{\Gamma}_{\rm sca}$ would be time-consuming. By analogy to $\boldsymbol{F}_{\rm sca}$, we appeal to the fact that the time-averaged torque exerted by the scattered field plus the time-averaged rate of transport of angular momentum to infinity by this field must sum to zero: $\langle \boldsymbol{\Gamma}_{\rm sca} \rangle + \langle \boldsymbol{\Gamma}_{\rm out} \rangle = 0$, where $\boldsymbol{\Gamma}_{\rm out}$ is the net rate of transport of angular momentum by the scattered radiation field across a fixed surface enclosing the target. In dyadic notation, the instantaneous angular momentum flux may be written

$$\boldsymbol{M} = \frac{1}{4\pi} \left[{\rm Re} \, (\boldsymbol{E}) \, {\rm Re} \, (\boldsymbol{E}) + {\rm Re} \, (\boldsymbol{B}) \, {\rm Re} \, (\boldsymbol{B}) - \frac{|{\rm Re} \, (\boldsymbol{E})|^2 + |{\rm Re} \, (\boldsymbol{B})|^2}{2} \, \mathbf{I} \right] \times \boldsymbol{r} \tag{25}$$

(Jackson 1975, p. 264, problem 6.11), where $\mathbf{I}$ is the unit dyadic. Integrating $\boldsymbol{M}$ over a spherical surface of radius r,

$$\boldsymbol{\Gamma}_{\rm out} = \int_S r^3 \, \frac{d\Omega}{4\pi} \, \hat{\boldsymbol{n}} \cdot [{\rm Re} \, (\boldsymbol{E}) \, {\rm Re} \, (\boldsymbol{E}) + {\rm Re} \, (\boldsymbol{B}) \, {\rm Re} \, (\boldsymbol{B})] \times \hat{\boldsymbol{n}} \,. \tag{26}$$

Now, if $r \gg \lambda$, the field radiated by the oscillating dipoles has $|\hat{\boldsymbol{n}} \cdot \boldsymbol{E}_{\rm sca}| \propto r^{-2}$, $|\hat{\boldsymbol{n}} \cdot \boldsymbol{B}_{\rm sca}| \propto r^{-2}$, $|\boldsymbol{E}_{\rm sca} \times \hat{\boldsymbol{n}}| \propto r^{-1}$, and $|\boldsymbol{B}_{\rm sca} \times \hat{\boldsymbol{n}}| \propto r^{-1}$. Thus, we need retain only the leading-order terms in evaluating each of these quantities. Expanding $\boldsymbol{E}_{\rm sca}$ and $\boldsymbol{B}_{\rm sca}$ as shown in Appendix A, letting $r \to \infty$,

$$\langle \boldsymbol{\Gamma}_{\rm sca} \rangle = -\langle \boldsymbol{\Gamma}_{\rm out} \rangle = -\frac{k^4}{8\pi} \int d\Omega \, {\rm Re} \, (\boldsymbol{S}_E^* \boldsymbol{V}_B + \boldsymbol{S}_B^* \boldsymbol{V}_E) \,, \tag{27}$$

$$\boldsymbol{S}_E \equiv \sum_{j=1}^{N} \left[\boldsymbol{r}_j - (\hat{\boldsymbol{n}} \cdot \boldsymbol{r}_j)\hat{\boldsymbol{n}} - \frac{2i}{k} \, \hat{\boldsymbol{n}} \right] \cdot \boldsymbol{p}_j(0) \exp(-ik\hat{\boldsymbol{n}} \cdot \boldsymbol{r}_j) \,, \tag{28}$$

$$\boldsymbol{S}_B \equiv \hat{\boldsymbol{n}} \cdot \sum_{j=1}^{N} \boldsymbol{p}_j(0) \times \boldsymbol{r}_j \exp(-ik\hat{\boldsymbol{n}} \cdot \boldsymbol{r}_j) \,, \tag{29}$$

$$\boldsymbol{V}_E \equiv \sum_{j=1}^{N} \{ \boldsymbol{p}_j(0) - \hat{\boldsymbol{n}}[\hat{\boldsymbol{n}} \cdot \boldsymbol{p}_j(0)] \} \exp(-ik\hat{\boldsymbol{n}} \cdot \boldsymbol{r}_j) \,, \tag{30}$$

$$\boldsymbol{V}_B \equiv \sum_{j=1}^{N} \boldsymbol{p}_j(0) \times \hat{\boldsymbol{n}} \exp(-ik\hat{\boldsymbol{n}} \cdot \boldsymbol{r}_j) \,, \tag{31}$$

$$= -\hat{\boldsymbol{n}} \times \boldsymbol{V}_E \,. \tag{32}$$

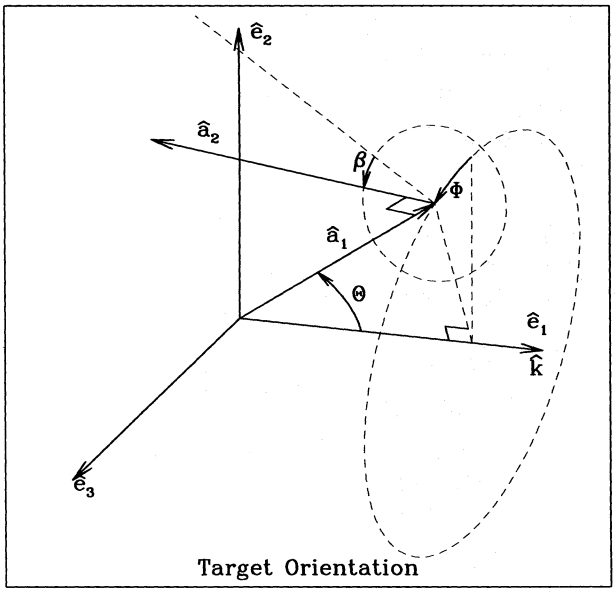

FIG. 2.—Grain orientation in "scattering coordinates"

Noting that for pure right-handed circularly polarized radiation, the time-averaged angular momentum flux is just $|\boldsymbol{E}_{\rm inc,0}|^2\hat{\boldsymbol{k}}/8\pi k$ (easily seen by noting that each photon carries angular momentum $\hbar$), it is convenient to define a dimensionless "torque efficiency vector" $\boldsymbol{Q}_\Gamma \equiv \boldsymbol{Q}_{\Gamma,\rm inc} + \boldsymbol{Q}_{\Gamma,\rm sca}$ such that the time-averaged torque

$$\langle \boldsymbol{\Gamma}_{\rm rad}\rangle = \langle \boldsymbol{\Gamma}_{\rm inc}\rangle + \langle \boldsymbol{\Gamma}_{\rm sca}\rangle = \boldsymbol{Q}_\Gamma \pi a_{\rm eff}^2 \frac{|\boldsymbol{E}_{\rm inc,0}|^2}{8\pi k}$$

$$= \pi a_{\rm eff}^2 u_{\rm rad} \frac{\lambda}{2\pi} \boldsymbol{Q}_\Gamma , \qquad (33)$$

where $u_{\rm rad} = |\boldsymbol{E}_{\rm inc,0}|^2/8\pi$ is the time-averaged energy density of the incident radiation. Clearly, we have

$$\boldsymbol{Q}_{\Gamma,\rm inc} = \frac{4k}{a_{\rm eff}^2 |\boldsymbol{E}_{\rm inc,0}|^2} \,{\rm Re}\left\{ \sum_{j=1}^{N} \boldsymbol{p}_j^*(0) \times \boldsymbol{E}_{\rm inc,0} e^{i\boldsymbol{k}\cdot\boldsymbol{r}_j} - i\boldsymbol{k} \times \sum_{j=1}^{N} \boldsymbol{r}_j [\boldsymbol{p}_j^*(0) \cdot \boldsymbol{E}_{\rm inc,0}] e^{i\boldsymbol{k}\cdot\boldsymbol{r}_j} \right\}, \qquad (34)$$

$$\boldsymbol{Q}_{\Gamma,\rm sca} = \frac{-k^5}{\pi a_{\rm eff}^2 |\boldsymbol{E}_{\rm inc,0}|^2} \int d\Omega \,{\rm Re}\,(\boldsymbol{S}_E^* \boldsymbol{V}_B + \boldsymbol{S}_B^* \boldsymbol{V}_E) . \qquad (35)$$

The direction and magnitude of $\boldsymbol{Q}_\Gamma$ depends on the grain orientation and on the direction of propagation and polarization of the incident radiation.

It is clear that for right-hand circularly polarized radiation with $\lambda \gg a_{\rm eff}$, we will have $\boldsymbol{Q}_\Gamma \approx Q_{\rm abs}\hat{\boldsymbol{k}}$.

5. TARGET ORIENTATION

It is necessary to specify the orientation of the target relative to the incident radiation. Let the target contain two axes $\hat{\boldsymbol{a}}_1$ and $\hat{\boldsymbol{a}}_2$ (with $\hat{\boldsymbol{a}}_1 \cdot \hat{\boldsymbol{a}}_2 = 0$), which are fixed relative to the target. Let us further suppose that $\hat{\boldsymbol{a}}_1$, $\hat{\boldsymbol{a}}_2$, and $\hat{\boldsymbol{a}}_3 = \hat{\boldsymbol{a}}_1 \times \hat{\boldsymbol{a}}_2$ are the principal axes of the target's moment of inertia tensor, with moments of inertia $I_1 \geq I_2 \geq I_3$ about these axes. The grain orientation is completely specified by the orientations of any two nonparallel fixed axes, in particular $\hat{\boldsymbol{a}}_1$ and $\hat{\boldsymbol{a}}_2$.

We define a "scattering frame," defined by unit vectors $\hat{\boldsymbol{e}}_1 = \hat{\boldsymbol{k}}$, $\hat{\boldsymbol{e}}_2 \perp \hat{\boldsymbol{e}}_1$, and $\hat{\boldsymbol{e}}_3 = \hat{\boldsymbol{e}}_1 \times \hat{\boldsymbol{e}}_2$. Three angles are required to specify the target orientation. The orientation of $\hat{\boldsymbol{a}}_1$ in the scattering frame is described by the two angles $\Theta \in [0, \pi]$ and $\Phi \in [0, 2\pi]$, where

$$\hat{\boldsymbol{a}}_1 = \cos\Theta\hat{\boldsymbol{e}}_1 + \sin\Theta\cos\Phi\hat{\boldsymbol{e}}_2 + \sin\Theta\sin\Phi\hat{\boldsymbol{e}}_3 . \qquad (36)$$

A third angle $\beta \in [0, 2\pi]$ describes rotations of the target axis $\hat{\boldsymbol{a}}_2$ around $\hat{\boldsymbol{a}}_1$:

$$\hat{\boldsymbol{a}}_2 = -\sin\Theta\cos\beta\hat{\boldsymbol{e}}_1 + (\cos\Theta\cos\beta\cos\Phi - \sin\beta\sin\Phi)\hat{\boldsymbol{e}}_2 + (\cos\Theta\cos\beta\sin\Phi + \sin\beta\cos\Phi)\hat{\boldsymbol{e}}_3 . \qquad (37)$$

The target orientation in the scattering frame is illustrated in Figure 2.

6. COMPUTATIONS FOR ONE SHAPE

We consider one specific grain shape. This shape, shown in Figure 3, is not intended to be realistic, but is chosen to be (1) easily described, (2) asymmetric, and (3) well suited to representation by a cubic array of point dipoles. The shape chosen is an assembly of 13 identical cubes. The coordinates of these cubes (in units of cube width) are listed in Table 1. The first eight cubes are arranged to form a single larger cube; the remaining five cubes are attached to the central eight cubes.

Let the eigenvalues $I_1 \geq I_2 \geq I_3$ of the moment of inertia tensor be written

$$I_j = \frac{2}{5}\alpha_j M a_{\rm eff}^2 = \frac{8\pi}{15}\alpha_j \rho a_{\rm eff}^5, \qquad (38)$$

where ρ is the solid density, and α_j are geometric factors. A sphere has $\alpha_j = 1$; a 2:2:1 rectangular solid ("brick") has

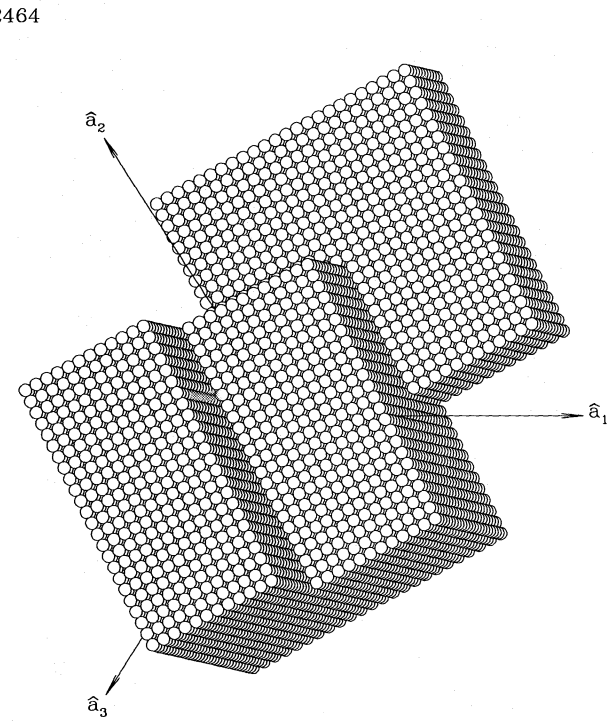

FIG. 3.—Representative irregular grain shape. The principal axes $\hat{\boldsymbol{a}}_1$, $\hat{\boldsymbol{a}}_2$, and $\hat{\boldsymbol{a}}_3$ are shown.

TABLE 1

TARGET GEOMETRY: COORDINATES OF CONSTITUENT BLOCKS

j	x_j	y_j	z_j
1	0	1	0
2	0	1	1
3	0	2	0
4	0	2	1
5	1	1	0
6	1	1	1
7	1	2	0
8	1	2	1
9	0	0	1
10	0	0	2
11	0	1	2
12	2	1	0
13	2	2	0

$\alpha_1 = (5/3)(\pi/3)^{2/3} = 1.719$, $\alpha_2 = \alpha_3 = (25/24)(\pi/3)^{2/3} = 1.074$. The principal axes $\hat{\boldsymbol{a}}_j$ and factors α_j for our adopted grain geometry are given in Table 2.

Let $T_{\rm gr}$ be the grain temperature. Purcell (1979) has shown that if the grain is spinning with angular momentum $\boldsymbol{J}$, and $J^2 \gg I_1 kT_{\rm gr}$, then viscoelastic damping and Barnett effect damping will rapidly bring the grain's principal axis $\hat{\boldsymbol{a}}_1$ into alignment with $\boldsymbol{J}$. In our discussion below we will therefore assume that $\hat{\boldsymbol{a}}_1$ is at all times perfectly aligned with the angular momentum $\boldsymbol{J}$ of the grain. The grain rotation period will be short compared to all other dynamical timescales, so it is appropriate to average the forces and torques over the grain rotation angle β, and henceforth we will discuss only the "β-averaged" efficiency vectors $\boldsymbol{Q}_{\rm pr}(\Theta, \Phi)$ and $\boldsymbol{Q}_\Gamma(\Theta, \Phi)$.

We have carried out scattering calculations for grains with the shape shown in Figure 3, the refractive index of "astronomical silicate" (Draine & Lee 1984)[2] and effective radii $a_{\rm eff} = 0.2$, 0.05, and 0.02 μm. The computations were carried out using the discrete dipole approximation program DDSCAT.5a.[3] The targets were represented by arrays of $N = 6656$, 22464, and 53248 dipoles; in each case, N was taken to be large enough to satisfy the validity criterion $|m|kd < 1$ (Draine & Flatau 1994), where $m(\omega)$ is the complex refractive index, and $d = (4\pi/3N)^{1/3} a_{\rm eff}$ is the interdipole spacing. Lattice dispersion relation theory (Draine & Goodman 1993) was used to determine the optimal choice of dipole polarizabilities at each wavelength. The computations employed FFT techniques (Goodman et al. 1991) and a stabilized version of the biconjugate gradients method (Flatau 1996); nevertheless, the computational demands were substantial, because of the need to compute scattering for many different wavelengths and orientations. For example, determining the scattering properties for one orientation and two polarization states for the $a_{\rm eff} = 0.2$ μm target at a single wavelength $\lambda = 0.4$ μm, with the target represented by $N = 22464$ dipoles, required 720 CPU seconds on a Sun-10 computer with a 125 MHz Hypersparc CPU. For the $a_{\rm eff} = 0.2$ μm grain, computations were carried out for 26 distinct wavelengths (from 0.1 to 20 μm) and 285 orientations (15 values of β for each of 19 values of Θ), requiring $\sim$2000 CPU hours.

TABLE 2

TARGET PRINCIPAL AXES $\hat{\boldsymbol{a}}_j$ AND FACTORS α_j

j	$(\hat{\boldsymbol{a}}_j)_x$	$(\hat{\boldsymbol{a}}_j)_y$	$(\hat{\boldsymbol{a}}_j)_z$	α_j
1	0.4488	0.4357	0.7802	1.745
2	0.6673	−0.7441	0.0317	1.610
3	0.5944	0.5064	−0.6247	0.876

[2] This dielectric function may be obtained by anonymous ftp to astro.princeton.edu, file draine/dust/eps.Sil.

[3] The Fortran program DDSCAT.5a is available from B. T. Draine and P. J. Flatau; contact draine@astro.princeton.edu for further information.

Consider a grain spinning around axis $\hat{\boldsymbol{a}}_1$, with $\hat{\boldsymbol{a}}_1 \perp \boldsymbol{k}$. In Figure 4 we show

$$Q_{\rm ext} \equiv \frac{C_{\rm ext}(\boldsymbol{E} \perp \hat{\boldsymbol{a}}_1) + C_{\rm ext}(\boldsymbol{E} \parallel \hat{\boldsymbol{a}}_1)}{2\pi a_{\rm eff}^2}, \quad (39)$$

$$Q_{\rm pol} \equiv \frac{C_{\rm ext}(\boldsymbol{E} \perp \hat{\boldsymbol{a}}_1) - C_{\rm ext}(\boldsymbol{E} \parallel \hat{\boldsymbol{a}}_1)}{\pi a_{\rm eff}^2}, \quad (40)$$

where $C_{\rm ext}$ is the extinction cross section averaged over grain rotation angle β. We see that the polarization cross section for the $a_{\rm eff} = 0.2$ μm grain peaks near $\lambda = 0.5$ μm. Grains of approximately this size would therefore be suitable for producing the bulk of the observed interstellar polarization, which tends to peak near $\lambda \approx 0.55$ μm. The $a_{\rm eff} = 0.05$ μm grain, on the other hand, is most effective at polarizing near $\lambda = 0.2$ μm (see Fig. 5); the observed wavelength dependence of interstellar polarization indicates that grains of this size are *not* appreciably aligned in the interstellar medium (Kim & Martin 1994b).

We can restrict our calculations to $\Phi = 0$; for other values of Φ, the efficiency vectors $\boldsymbol{Q}$ may be obtained by a simple rotation:

$$\begin{aligned}\boldsymbol{Q}(\Theta, \Phi) = {} & \boldsymbol{Q}(\Theta, 0) \cdot \hat{\boldsymbol{e}}_1 \hat{\boldsymbol{e}}_1 \\ & + \boldsymbol{Q}(\Theta, 0) \cdot \hat{\boldsymbol{e}}_2 (\hat{\boldsymbol{e}}_2 \cos\Phi + \hat{\boldsymbol{e}}_3 \sin\Phi) \\ & + \boldsymbol{Q}(\Theta, 0) \cdot \hat{\boldsymbol{e}}_3 (\hat{\boldsymbol{e}}_3 \cos\Phi - \hat{\boldsymbol{e}}_2 \sin\Phi) . \quad (41)\end{aligned}$$

Let $(\boldsymbol{Q}_{\rm pr}^1, \boldsymbol{Q}_{\rm pr}^2)$ and $(\boldsymbol{Q}_\Gamma^1, \boldsymbol{Q}_\Gamma^2)$ be the radiation pressure and radiation torque efficiency vectors for polarization states 1

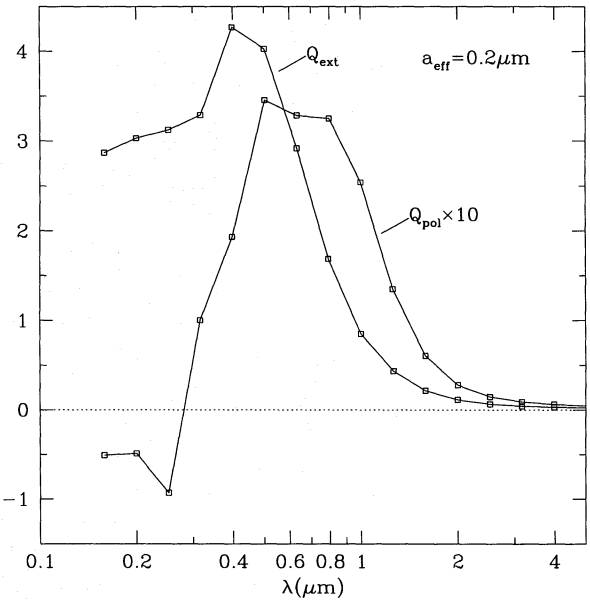

FIG. 4.—Extinction and polarization efficiency factors for the grain shape shown in Fig. 3, with $a_{\rm eff} = 0.2$ μm, spinning around the principal axis $\hat{\boldsymbol{a}}_1$, with radiation propagating perpendicular to $\hat{\boldsymbol{a}}_1$. The polarization cross section peaks at $\lambda = 0.5$ μm, with $Q_{\rm pol}/Q_{\rm ext} = 0.086$ for this particular grain.

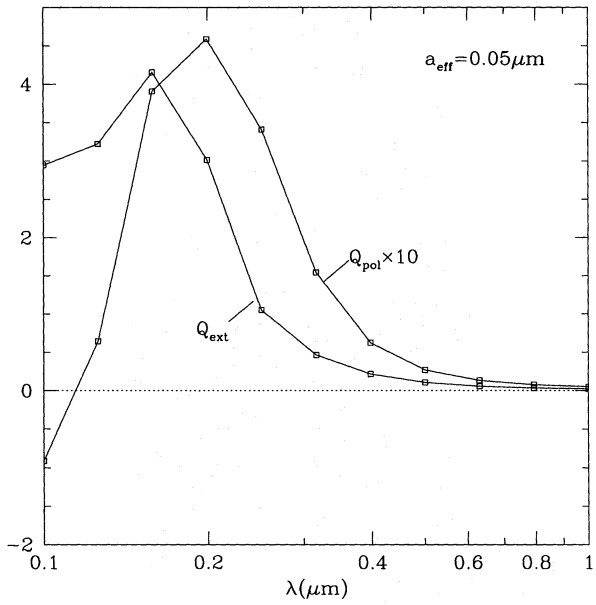

FIG. 5.—Same as Fig. 4, but for $a_{eff} = 0.05$ μm, with Q_{pol} peaking at $\lambda = 0.2$ μm, with $Q_{pol}/Q_{ext} = 0.15$.

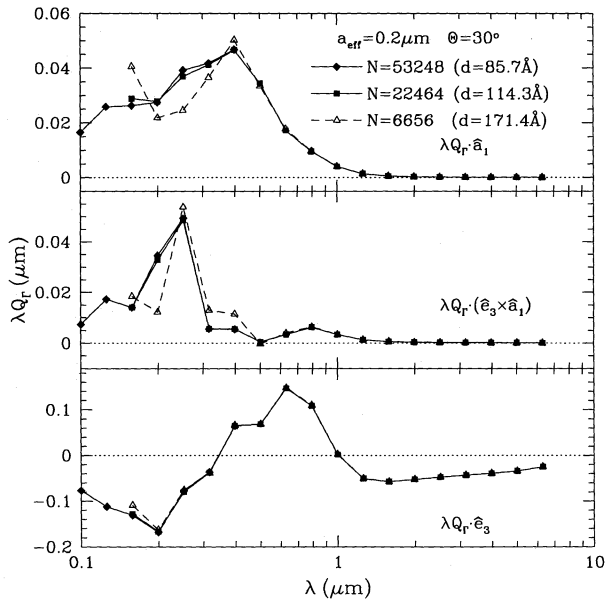

FIG. 7.—Three components of λQ_Γ for $\Theta = 30°$, as a function of λ, for an $a_{eff} = 0.2$ μm grain. Results are shown for DDA calculations using $N = 6656$, 22464, and 53248 dipoles. It is seen that the $N = 22464$ dipole array provides a good approximation to the target for $\lambda \gtrsim 0.15$ μm.

and 2 (these can be any two orthogonal polarization states, e.g., two linear polarization states, or left- and right-handed circular polarization states). For unpolarized incident radiation (i.e., equal amounts of two orthogonal polarization states), we have efficiency vectors

$$\boldsymbol{Q}_{pr}^{un} = \tfrac{1}{2}(\boldsymbol{Q}_{pr}^{1} + \boldsymbol{Q}_{pr}^{2}) , \quad (42)$$

$$\boldsymbol{Q}_{\Gamma}^{un} = \tfrac{1}{2}(\boldsymbol{Q}_{\Gamma}^{1} + \boldsymbol{Q}_{\Gamma}^{2}) . \quad (43)$$

Henceforth in this paper we will be concerned only with unpolarized radiation, and we will omit the "un" superscript. In Figure 6 we show our results for the component of $\boldsymbol{Q}_{pr}(\Theta, 0)$ along $\hat{\boldsymbol{k}}$, as a function of λ, for several values of Θ. This is, of course, just the usual "radiation pressure efficiency factor" $[Q_{abs} + (1 - \langle\cos\Theta\rangle)Q_{sca}]$. We see the expected tendency for $\boldsymbol{Q}_{pr} \cdot \hat{\boldsymbol{k}}$ to be small when $\lambda \gg a_{eff}$, and to be of order unity when $2\pi a_{eff}/\lambda \gtrsim 1$ (i.e., $\lambda \lesssim 1$ μm for $a_{eff} = 0.2$ μm, and $\lambda \lesssim 0.3$ μm for $a_{eff} = 0.05$ μm.

In Figure 7 we show the three components of the radiation torque efficiency vector $\boldsymbol{Q}_\Gamma$ for the $a_{eff} = 0.2$ μm target oriented at $\Theta = 30°$. For $\lambda \geq 0.1585$ μm, results are shown for three different dipole arrays, with $N = 6656$, 22464, and 53248 dipoles, with interdipole separations $d = 171$, 114,

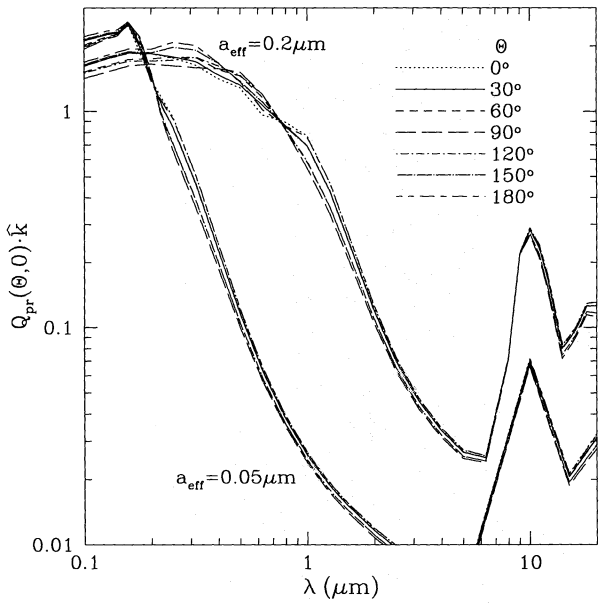

FIG. 6.—Component of the radiation pressure efficiency vector $\boldsymbol{Q}_{pr}(\Theta, 0)$ along $\hat{\boldsymbol{k}}$, the propagation direction of the incident radiation, as a function of wavelength λ, for several values of the angle Θ between $\hat{\boldsymbol{k}}$ and the grain axis $\hat{\boldsymbol{a}}_1$, and for two different grain sizes, $a_{eff} = 0.2$ and 0.05 μm. $\boldsymbol{Q}_{pr}$ is averaged over the angle β measuring rotations of the grain around $\hat{\boldsymbol{a}}_1$. The peak near 10 μm is the silicate absorption feature.

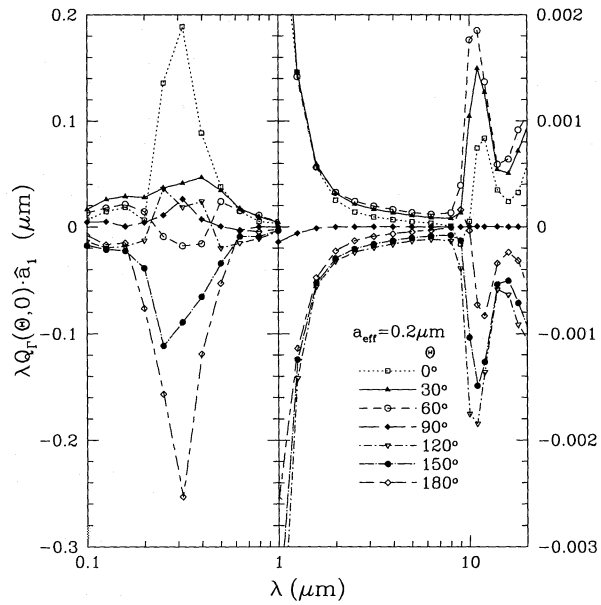

FIG. 8.—$\lambda\boldsymbol{Q}_\Gamma(\Theta, 0) \cdot \hat{\boldsymbol{a}}_1$, where $\boldsymbol{Q}_\Gamma$ is the radiation torque efficiency vector and $\hat{\boldsymbol{a}}_1$ is the principal axis with the largest moment of inertia, for $a_{eff} = 0.2$ μm grain and various values of the angle Θ between $\hat{\boldsymbol{a}}_1$ and $\hat{\boldsymbol{k}}$.

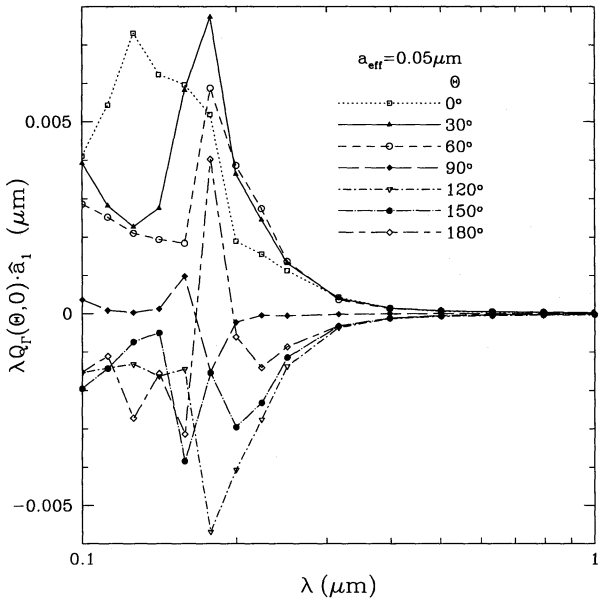

FIG. 9.—Same as Fig. 8 but for $a_{\rm eff} = 0.05$ μm

and 85.7 Å. At $\lambda = 0.1585$ μm, we have $m = 2.153 + 0.263i$, so that for the three dipole arrays at this wavelength we have $|m|kd = 1.47$, 0.98, and 0.74. We see that the DDA calculations appear to have converged when $|m|kd < 1$. At the shortest wavelength, $\lambda = 0.1$ μm, we have $m = 1.545 + 0.956i$, and for the $N = 53248$ array we have $|m|kd = 0.98$, marginally satisfying our validity criterion.

Figures 8 and 9 show, as a function of λ, the component of $\boldsymbol{Q}_\Gamma$ along the principal axis $\hat{\boldsymbol{a}}_1$, about which we have assumed the grains to be spinning, for $a_{\rm eff} = 0.2$ and 0.05 μm grains. This component of $\boldsymbol{Q}_\Gamma$ will tend to spin up the grain if $\boldsymbol{Q}_\Gamma \cdot \hat{\boldsymbol{a}}_1/\boldsymbol{J} \cdot \hat{\boldsymbol{a}}_1 > 0$, or to spin it down if $\boldsymbol{Q}_\Gamma \cdot \hat{\boldsymbol{a}}_1/\boldsymbol{J} \cdot \hat{\boldsymbol{a}}_1 < 0$.

7. INTERSTELLAR GRAINS

7.1. *Radiation Fields*

The average interstellar radiation field (ISRF) spectrum in the solar neighborhood has been estimated to be (Mezger, Mathis, & Panagia 1982; Mathis, Mezger, & Panagia 1983)

$$\lambda u_{{\rm ISRF},\lambda} = U(\lambda) \qquad \text{for } \lambda < 2460 \text{ Å} \quad (44)$$

$$= \frac{4\pi\lambda}{c} \sum_{i=1}^{3} W_i B_\lambda(T_i) \qquad \text{for } \lambda > 2460 \text{ Å}, \quad (45)$$

where the ultraviolet function

$$U(\lambda) = \begin{cases} 0, & \text{for } \lambda < 912 \text{ Å or } \lambda > 2460 \text{ Å}, \\ 1.287 \times 10^{-9}(\lambda/\mu{\rm m})^{4.4172} \text{ ergs cm}^{-3}, & \text{for } 912 - 1100 \text{ Å}, \\ 6.825 \times 10^{-13}(\lambda/\mu{\rm m}) \text{ ergs cm}^{-3}, & \text{for } 1100 - 1340 \text{ Å}, \\ 2.373 \times 10^{-14}(\lambda/\mu{\rm m})^{-0.6678} \text{ ergs cm}^{-3}, & \text{for } 1340 - 2460 \text{ Å}. \end{cases} \quad (46)$$

The three blackbody components are indicated in Table 3, where we also provide values of u and $\bar{\lambda}$ for each of the four spectral components, where

$$u \equiv \int u_\lambda \, d\lambda, \quad (47)$$

$$\bar{\lambda} \equiv \frac{\int \lambda u_\lambda \, d\lambda}{\int u_\lambda \, d\lambda}. \quad (48)$$

The total starlight energy density is $u_{\rm ISRF} = 8.64 \times 10^{-13}$ ergs cm^{-3}. We expect appreciable anisotropy in the typical interstellar radiation field: generally, there will be more starlight from the direction of the Galactic center, the nearest bright star or association may be important, and nearby dust may attenuate the starlight over one part of the sky. We define an anisotropy parameter γ, such that the net Poynting flux is $\gamma u_{\rm rad} c$, where $u_{\rm rad}$ is the total energy density of radiation. We assume $\gamma \approx 0.1$ to be a characteristic value. In our discussions below we will represent the radiation field as an isotropic component with energy density $(1 - \gamma)u_{\rm rad}$ plus a unidirectional component with energy density $\gamma u_{\rm rad}$.

7.2. *Radiative Forces and Torques Due to Starlight*

7.2.1. *Unidirectional Radiation*

For a grain subject to a unidirectional radiation field with energy density $\gamma u_{\rm rad}$, the force and torque on the grain are

$$\boldsymbol{F}_{\rm rad} = \pi a_{\rm eff}^2 \gamma u_{\rm rad} \langle \boldsymbol{Q}_{\rm pr}(\Theta, \Phi) \rangle, \quad (49)$$

$$\boldsymbol{\Gamma}_{\rm rad} = \pi a_{\rm eff}^2 \gamma u_{\rm rad} \frac{\bar{\lambda}}{2\pi} \langle \boldsymbol{Q}_\Gamma(\Theta, \Phi) \rangle, \quad (50)$$

where angle brackets now denote spectral averaging:

$$\langle \boldsymbol{Q}(\Theta, \Phi) \rangle \equiv \frac{\int \boldsymbol{Q}(\Theta, \Phi) \lambda u_\lambda \, d\lambda}{\int \lambda u_\lambda \, d\lambda}. \quad (51)$$

In Table 4 we present values of $\hat{\boldsymbol{a}}_1 \cdot \langle \boldsymbol{Q}_{\rm pr} \rangle$ and $\hat{\boldsymbol{a}}_1 \cdot \langle \boldsymbol{Q}_{\rm pr} \rangle$ for $(\Theta, \Phi) = (0, 0)$, with the spectral averages evaluated for each of the u_λ in Table 3, for three grain sizes, $a_{\rm eff} = 0.02$, 0.05, and 0.2 μm. Note that the torque efficiencies $\langle \boldsymbol{Q}_\Gamma \rangle$

TABLE 3

INTERSTELLAR RADIATION FIELD COMPONENTS

Radiation Field	$u_{\rm rad}$ (ergs cm^{-3})	$\bar{\lambda}$ (μm)
UV [eq. (46)]	7.13×10^{-14}	0.1566
$W = 1 \times 10^{-14}$, $T = 7500$ K ($\lambda > 2460$ Å)	2.29×10^{-13}	0.7333
$W = 1.65 \times 10^{-13}$, $T = 4000$ K ($\lambda > 2460$ Å)	3.19×10^{-13}	1.3319
$W = 4 \times 10^{-13}$, $T = 3000$ K ($\lambda > 2460$ Å)	2.45×10^{-13}	1.7755
ISRF	8.64×10^{-13}	1.2021

TABLE 4

SILICATE GRAIN PROPERTIES

Parameter	$a_{\rm eff} = 0.02$ μm	$a_{\rm eff} = 0.05$ μm	$a_{\rm eff} = 0.2$ μm
$\langle Q_{\rm abs}\rangle_{\rm uv}$	0.758	1.254	1.100
$\langle Q_{\rm abs}\rangle_{7500\,\rm K}$	0.0150	0.0479	0.340
$\langle Q_{\rm abs}\rangle_{4000\,\rm K}$	0.00855	0.0234	0.163
$\langle Q_{\rm abs}\rangle_{3000\,\rm K}$	0.00664	0.0181	0.111
$\langle Q_{\rm abs}\rangle_{\rm ISRF}$	0.0716	0.130	0.273
$\langle Q_{\rm pr}^{\rm iso}\rangle_{\rm uv}$	1.31×10^{-3}	-6.82×10^{-3}	-4.12×10^{-3}
$\langle Q_{\rm pr}^{\rm iso}\rangle_{7500}$	$2. \times 10^{-7}$	1.29×10^{-4}	-2.25×10^{-2}
$\langle Q_{\rm pr}^{\rm iso}\rangle_{4000}$	...	5.4×10^{-6}	3.76×10^{-3}
$\langle Q_{\rm pr}^{\rm iso}\rangle_{3000}$	...	...	-6.53×10^{-4}
$\langle Q_{\rm pr}^{\rm iso}\rangle_{\rm ISRF}$	1.1×10^{-4}	-5.25×10^{-4}	-7.86×10^{-3}
$\langle Q_\Gamma^{\rm iso}\rangle_{\rm uv}$	2.64×10^{-4}	2.52×10^{-3}	5.34×10^{-3}
$\langle Q_\Gamma^{\rm iso}\rangle_{7500\,\rm K}$	4.43×10^{-8}	2.04×10^{-6}	5.31×10^{-4}
$\langle Q_\Gamma^{\rm iso}\rangle_{4000\,\rm K}$	1.41×10^{-8}	1.89×10^{-7}	1.06×10^{-4}
$\langle Q_\Gamma^{\rm iso}\rangle_{3000\,\rm K}$	9.03×10^{-9}	6.48×10^{-8}	2.99×10^{-5}
$\langle Q_\Gamma^{\rm iso}\rangle_{\rm ISRF}$	2.84×10^{-6}	2.75×10^{-5}	1.99×10^{-4}
$\hat{k} \cdot \langle Q_{\rm pr}\rangle_{\rm uv}\ (\Theta = 0°)$	1.141	1.860	1.438
$\hat{k} \cdot \langle Q_{\rm pr}\rangle_{7500\,\rm K}\ (\Theta = 0°)$	0.0203	0.184	1.117
$\hat{k} \cdot \langle Q_{\rm pr}\rangle_{4000\,\rm K}\ (\Theta = 0°)$	0.00965	0.0454	0.651
$\hat{k} \cdot \langle Q_{\rm pr}\rangle_{3000\,\rm K}\ (\Theta = 0°)$	0.00724	0.0257	0.457
$\hat{k} \cdot \langle Q_{\rm pr}\rangle_{\rm ISRF}\ (\Theta = 0°)$	0.105	0.226	0.784
$\hat{a}_1 \cdot \langle Q_\Gamma\rangle_{\rm uv}\ (\Theta = 0°)$	2.54×10^{-3}	2.94×10^{-2}	7.01×10^{-2}
$\hat{a}_1 \cdot \langle Q_\Gamma\rangle_{\rm uv}\ (\Theta = 60°)$	3.55×10^{-3}	1.67×10^{-2}	9.06×10^{-2}
$\hat{a}_1 \cdot \langle Q_\Gamma\rangle_{7000\,\rm K}\ (\Theta = 0°)$	6.01×10^{-6}	2.00×10^{-4}	7.45×10^{-2}
$\hat{a}_1 \cdot \langle Q_\Gamma\rangle_{7000\,\rm K}\ (\Theta = 60°)$	1.22×10^{-5}	2.16×10^{-4}	4.38×10^{-3}
$\hat{a}_1 \cdot \langle Q_\Gamma\rangle_{4000\,\rm K}\ (\Theta = 0°)$	1.60×10^{-6}	1.88×10^{-5}	7.78×10^{-3}
$\hat{a}_1 \cdot \langle Q_\Gamma\rangle_{4000\,\rm K}\ (\Theta = 60°)$	3.88×10^{-6}	2.90×10^{-5}	4.39×10^{-3}
$\hat{a}_1 \cdot \langle Q_\Gamma\rangle_{3000\,\rm K}\ (\Theta = 0°)$	9.01×10^{-7}	7.36×10^{-6}	2.07×10^{-3}
$\hat{a}_1 \cdot \langle Q_\Gamma\rangle_{3000\,\rm K}\ (\Theta = 60°)$	2.27×10^{-6}	1.52×10^{-5}	2.07×10^{-3}
$\hat{a}_1 \cdot \langle Q_\Gamma\rangle_{\rm ISRF}\ (\Theta = 0°)$	2.93×10^{-5}	3.59×10^{-4}	1.69×10^{-2}
$\hat{a}_1 \cdot \langle Q_\Gamma\rangle_{\rm ISRF}\ (\Theta = 60°)$	4.26×10^{-5}	2.33×10^{-4}	4.35×10^{-3}

become very small as the grain size is decreased below ~0.1 μm.

In Figures 10–15 we show the three vector components of $\langle \boldsymbol{Q}_\Gamma(\Theta, 0)\rangle$, for the $a_{\rm eff} = 0.2$ and $a_{\rm eff} = 0.05$ μm grains; results are again shown for each of the u_λ in Table 3.

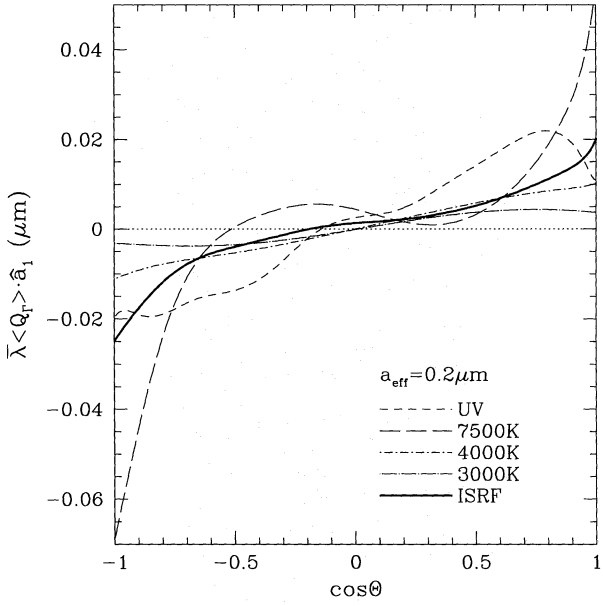

FIG. 10.—Component of the spectrum-averaged radiation torque efficiency vector $\langle \boldsymbol{Q}_\Gamma\rangle$ along $\hat{a}_1$ for $a_{\rm eff} = 0.2$ μm grain, multiplied by $\bar{\lambda}$, as a function of cos Θ, for the five radiation fields of Table 3. $\langle \boldsymbol{Q}_\Gamma\rangle$ is averaged over rotations of the grain around $\hat{a}_1$.

7.2.2. *Isotropic Radiation*

Consider a grain spinning around axis $\hat{a}_1$. An isotropic radiation field will result in a force $\boldsymbol{F}_{\rm rad}$ and torque $\boldsymbol{\Gamma}_{\rm rad}$ on the grain that are each fixed in body coordinates. Because of the grain rotation, in inertial coordinates the only component of the force or torque that will not average to zero

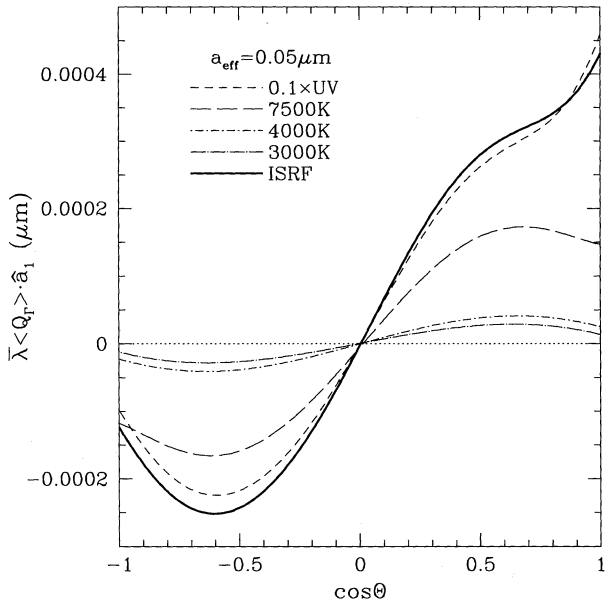

FIG. 11.—Same as Fig. 10 but for $a_{\rm eff} = 0.05$ μm. The results for the "UV" radiation field have been multiplied by a factor 0.1.

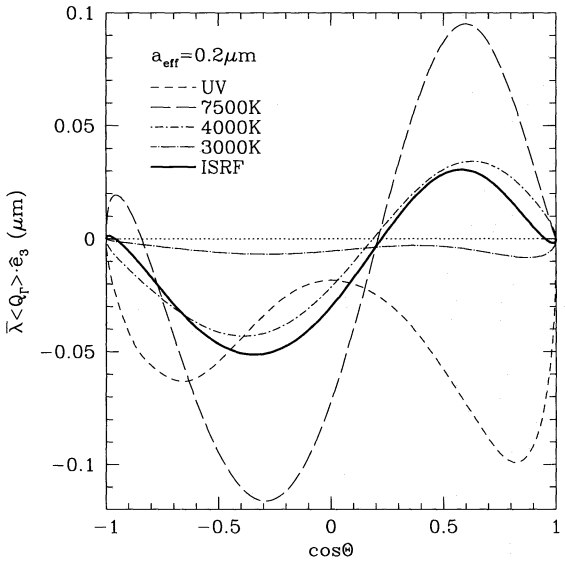

FIG. 12.—Same as Fig. 10 except showing the component of the spectrum-averaged radiation torque efficiency vector along $\hat{e}_3$. This torque would tend to cause precession of $\boldsymbol{J}$ around $\hat{\boldsymbol{k}}$.

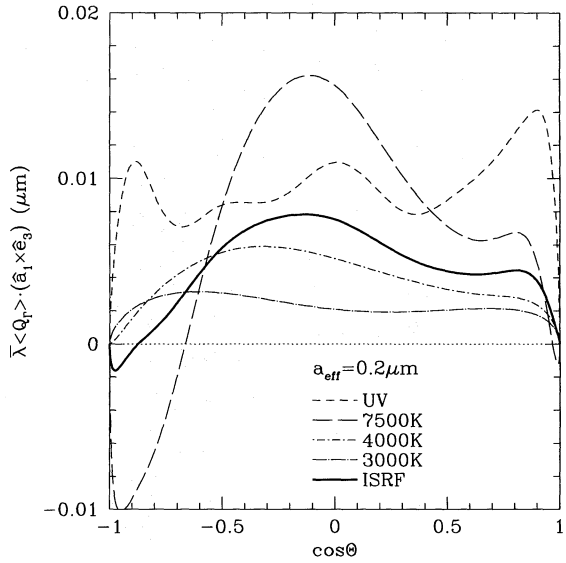

FIG. 14.—Same as Fig. 10 except showing the component of the spectrum-averaged torque efficiency vector $\langle \boldsymbol{Q}_\Gamma\rangle$ along $\hat{\boldsymbol{a}}_1 \times \hat{\boldsymbol{e}}_3$, for a_{eff} = 0.2 μm grain. If $\hat{\boldsymbol{a}}_1 \parallel \boldsymbol{J}$, this torque (if positive) would tend to cause alignment of $\boldsymbol{J}$ with $\hat{\boldsymbol{k}}$.

will be the component parallel to the rotation axis $\hat{\boldsymbol{a}}_1$:

$$\boldsymbol{F}_{rad} = \pi a_{eff}^2(1-\gamma)u_{rad}\langle Q_{pr}^{iso}\rangle\hat{\boldsymbol{a}}_1, \quad (52)$$

$$\boldsymbol{\Gamma}_{rad} = \pi a_{eff}^2(1-\gamma)u_{rad}\frac{\bar{\lambda}}{2\pi}\langle Q_\Gamma^{iso}\rangle\hat{\boldsymbol{a}}_1, \quad (53)$$

where

$$\langle Q^{iso}\rangle \equiv \frac{1}{2}\int_0^\pi \sin\Theta\, d\Theta\, \hat{\boldsymbol{a}}_1\cdot\langle \boldsymbol{Q}(\Theta,0)\rangle \quad (54)$$

is the effective efficiency vector for a grain spinning around $\hat{\boldsymbol{a}}_1$ and exposed to isotropic radiation. Values of $\langle Q_{pr}^{iso}\rangle$ and $\langle Q_\Gamma^{iso}\rangle$ are given in Table 4.

7.3. *Rotational Damping*

For a grain in neutral gas of hydrogen density $n_H = n(H) + 2n(H_2)$ and temperature T, the gas drag torque on a grain with angular velocity ω around axis $\hat{\boldsymbol{a}}_1$ may be written

$$\boldsymbol{\Gamma}_{drag,gas} = -\tfrac{2}{3}\delta n_H(1.2)(8\pi m_H kT)^{1/2}a_{eff}^4\,\omega\hat{\boldsymbol{a}}_1, \quad (55)$$

where m_H is the mass of an H atom. If all impinging atoms "stick" and then leave with negligible velocity relative to the local (moving) surface, then $\delta = 1$ for a sphere, and $\delta = 2(\pi/3)^{1/3} = 2.01$ for a 2:2:1 brick; in general, we expect $\delta \approx \alpha_1$. The factor 1.2 in equation (55) allows for the effects of helium with $n_{He} = 0.1n_H$.[4]

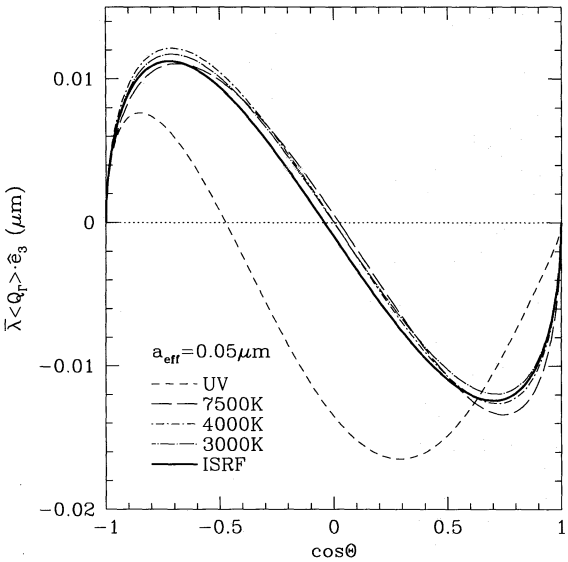

FIG. 13.—Same as Fig.12 except for a_{eff} = 0.05 μm

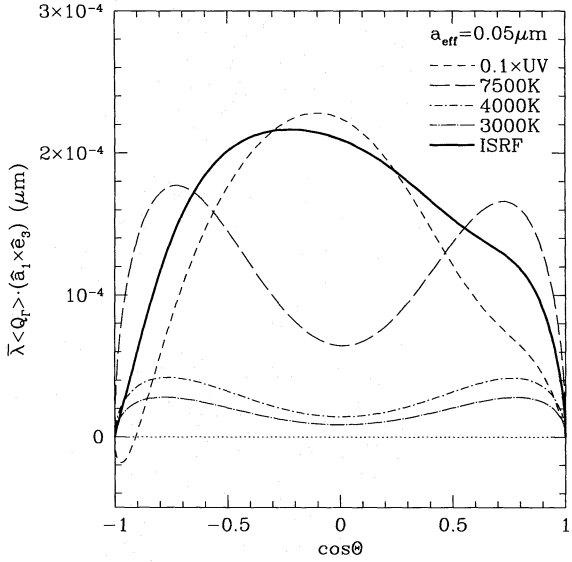

FIG. 15.—Same as Fig. 14 but for a_{eff} = 0.05 μm. The results for the "UV" radiation field have been multiplied by 0.1.

[4] We have assumed the H to be fully atomic; in fully molecular gas the factor 1.2 in equation (55) should be replaced by $2^{-1/2} + 0.2 = .907$.

The rotational damping time is

$$\tau_{\rm drag,gas} = \frac{\pi\alpha_1\rho a_{\rm eff}}{3\delta n_{\rm H}(2\pi m_{\rm H}kT)^{1/2}} = (8.74\times10^4\ {\rm yr}) \times \frac{\alpha_1}{\delta}\rho_3 a_{-5} T_2^{1/2}\left(\frac{3000\ {\rm cm^{-3}\ K}}{n_{\rm H}T}\right), \quad (56)$$

where $\rho_3 \equiv \rho/3$ g cm^{-3}, $a_{-5} \equiv a_{\rm eff}/10^{-5}$ cm, and $T_2 \equiv T/10^2$K.

In addition to collisions with gas atoms, there is rotational damping associated with absorption and emission of photons by the grain (Purcell & Spitzer 1971; Roberge, deGraff, & Flaherty 1993). If we assume that the grain is heated by starlight to a temperature T_d, and that $Q_{\rm abs} \propto \lambda^{-\beta}$ at wavelengths $\lambda \gtrsim 0.1hc/kT_d$, then the damping time due to thermal emission may be written

$$\tau_{\rm drag,em} = \frac{8\alpha_1(\beta+3)}{5}\frac{\zeta(\beta+4)}{\zeta(\beta+3)}\frac{\rho a_{\rm eff}^3(kT_d)^2}{\hbar^2 c u_{\rm rad}\langle Q_{\rm abs}\rangle} \quad (57)$$

$$= (1.60\times10^5\ {\rm yr})\frac{\alpha_1\rho_3 a_{-5}^3}{\langle Q_{\rm abs}\rangle}\left(\frac{T_d}{18\ {\rm K}}\right)^2\left(\frac{u_{\rm ISRF}}{u_{\rm rad}}\right), \quad (58)$$

where $\zeta(x)$ denotes the Riemann ζ-function,

$$\langle Q_{\rm abs}\rangle \equiv \frac{1}{u_{\rm rad}}\int u_\lambda Q_{\rm abs}(\lambda)d\lambda\ , \quad (59)$$

and we have assumed $\beta = 2$ in equation (58), as expected for simple models (Draine & Lee 1984) and as appears to be required by the far-infrared emission from dust in diffuse clouds (Draine 1994).[5] In equation (58) it is assumed that the radiated photons have angular momentum $\hbar$ relative to the grain center of mass; this will be true for radii $a \ll hc/kT_d = 800(18\ {\rm K}/T_d)\ \mu$m. There is additional damping associated with absorption of starlight photons, but it is smaller than the damping due to thermal emission by a factor $\sim T_d/T_{\rm rad} \approx 1/500$, where $T_{\rm rad}$ is the color temperature of the radiation responsible for heating the grain (Purcell 1979), and hence may be neglected. Values of $\langle Q_{\rm abs}\rangle$ are given in Table 4. The rotational damping time $\tau_{\rm drag}$ is given by

$$\tau_{\rm drag}^{-1} = \tau_{\rm drag,gas}^{-1} + \tau_{\rm drag,em}^{-1}\ . \quad (60)$$

8. SUPERTHERMAL ROTATION

8.1. H_2 *Formation*

The thermal rotation rate for a grain may be written

$$\omega_T^2 = \frac{15}{8\pi\alpha_1}\frac{kT}{\rho a_{\rm eff}^5}\ , \quad (61)$$

assuming rotation around $\hat{\boldsymbol{a}}_1$ with kinetic energy $kT/2$. Purcell (1979) pointed out that H_2 formation on the grain surface, taking place only at randomly located "active sites," would result in a large torque. The component of the torque perpendicular to the rotation axis $\hat{\boldsymbol{a}}_1$ would average to zero; for a 2:2:1 rectangular solid, Purcell estimated the component parallel to the rotation axis to be

$$\boldsymbol{\Gamma}_{H_2}\cdot\hat{\boldsymbol{a}}_1 = \frac{1}{3}\left(\frac{\pi}{3}\right)^{1/6} f n({\rm H})(2EkT)^{1/2}a_{\rm eff}^2\, l\, p(t)\ , \quad (62)$$

where n(H) is the density of H atoms in the gas, l^2 is the surface area per H_2 formation site on the grain surface, f is the fraction of arriving H atoms which depart as H_2, E is the kinetic energy of the departing H_2 molecules, and $p(t)$ is a random variable with time averages $\langle p(t)\rangle = 0$, $\langle p(t)p(t+\tau)\rangle = e^{-\tau/t_0}$, where t_0 is the "lifetime" of a surface recombination site.

If the only torques acting on the grain are those due to gas drag and H_2 formation, the grain will attain a rotation rate ω_{H_2}; the mean kinetic energy will exceed $0.5kT$ by a factor

$$\left(\frac{\omega_{H_2}}{\omega_T}\right)^2 = \frac{5\alpha_1 f^2}{216\delta^2}\left[\frac{n({\rm H})}{n_{\rm H}}\right]^2\frac{E}{kT}\frac{\rho a_{\rm eff}l^2}{m_{\rm H}}\left(\frac{\tau_{\rm drag}}{\tau_{\rm drag,gas}}\right)^2 \times\left(\frac{t_0}{t_0+\tau_{\rm drag}}\right) \quad (63)$$

(Purcell 1979).

8.2. *Radiative Torques*

If the grain is subject to a steady radiative torque

$$\boldsymbol{\Gamma}_{\rm rad} = \pi a_{\rm eff}^2 u_{\rm rad}\frac{\bar{\lambda}}{2\pi}[(1-\gamma)\langle Q_\Gamma^{\rm iso}\rangle + \gamma\langle\boldsymbol{Q}_\Gamma(\Theta)\rangle\cdot\hat{\boldsymbol{a}}_1]\hat{\boldsymbol{a}}_1 \quad (64)$$

along the rotation axis $\hat{\boldsymbol{a}}_1$, then, ignoring other sources of rotational excitation by the gas, we equate equations (55) and (64) to find that the grain will rotate around $\hat{\boldsymbol{a}}_1$ with an angular velocity

$$\omega_{\rm rad} = \frac{5\bar{\lambda}}{8\delta a_{\rm eff}^2}\left(\frac{kT}{8\pi m_{\rm H}}\right)^{1/2}\left(\frac{u_{\rm rad}}{n_{\rm H}kT}\right) \times[(1-\gamma)\langle Q_\Gamma^{\rm iso}\rangle + \gamma\langle\boldsymbol{Q}_\Gamma\rangle\cdot\hat{\boldsymbol{a}}_1]\left(\frac{\tau_{\rm drag}}{\tau_{\rm drag,gas}}\right). \quad (65)$$

We see that, in addition to $\langle Q_\Gamma^{\rm iso}\rangle$ and $\langle\boldsymbol{Q}_\Gamma\rangle\cdot\hat{\boldsymbol{a}}_1$, $\omega_{\rm rad}$ is determined by the ratio of radiation pressure to gas pressure ($u_{\rm rad}/n_{\rm H}kT$) and the anisotropy factor γ. The rotational kinetic energy will exceed $0.5kT$ by a factor

$$\left(\frac{\omega_{\rm rad}}{\omega_T}\right)^2 = \frac{5\alpha_1}{192\delta^2}\left(\frac{u_{\rm rad}}{n_{\rm H}kT}\right)^2\left(\frac{\rho a_{\rm eff}\bar{\lambda}^2}{m_{\rm H}}\right) \times[(1-\gamma)\langle Q_\Gamma^{\rm iso}\rangle + \gamma\langle\boldsymbol{Q}_\Gamma\rangle\cdot\hat{\boldsymbol{a}}_1]^2\left(\frac{\tau_{\rm drag}}{\tau_{\rm drag,gas}}\right)^2 \quad (66)$$

$$= 4.72\times10^9\frac{\alpha_1}{\delta^2}\rho_3 a_{-5}\left(\frac{u_{\rm rad}}{n_{\rm H}kT}\right)^2\left(\frac{\bar{\lambda}}{\mu{\rm m}}\right)^2 \times[(1-\gamma)\langle Q_\Gamma^{\rm iso}\rangle + \gamma\langle\boldsymbol{Q}_\Gamma\rangle\cdot\hat{\boldsymbol{a}}_1]^2\left(\frac{\tau_{\rm drag}}{\tau_{\rm drag,gas}}\right)^2. \quad (67)$$

8.3. *Diffuse Clouds*

In a diffuse cloud where the hydrogen is predominantly atomic, H_2 recombination on the grain surface will result in very rapid grain rotation. Values of $(\omega_{H_2}/\omega_T)^2$ are given in

[5] The damping time $\tau_{\rm drag,em}$ is insensitive to the precise value of β: the factor $(\beta+3)\zeta(\beta+4)/\zeta(\beta+3)$ decreases by only 22% if β is reduced from $\beta = 2$ to 1.

TABLE 5

SILICATE GRAINS IN DIFFUSE CLOUDS

Parameter	$a_{\rm eff} = 0.02$ μm	$a_{\rm eff} = 0.05$ μm	$a_{\rm eff} = 0.2$ μm
$\tau_{\rm drag,gas}$ (yr)	1.53×10^4	3.81×10^4	1.53×10^5
$\tau_{\rm drag,em}$ (yr)	3.12×10^4	2.68×10^5	8.18×10^6
$\tau_{\rm drag}$ (yr)	1.03×10^4	3.34×10^4	1.50×10^5
ω_T (rad s^{-1})	7.01×10^6	7.10×10^5	2.22×10^4
$(\omega_{H2}/\omega_T)^2$ for $t_0 = 10^4$ yr	2.10×10^2	4.16×10^2	5.65×10^2
$(\omega_{H2}/\omega_T)^2$ for $t_0 = 10^5$ yr	3.86×10^2	1.35×10^3	3.62×10^3
$(\omega_{H2}/\omega_T)^2$ for $t_0 = 10^6$ yr	4.22×10^2	1.75×10^3	7.86×10^3
$(\omega_{\rm rad}/\omega_T)^2$ for $\Theta = 0°$	3.56×10^{-2}	18.4	8.73×10^4
$(\omega_{\rm rad}/\omega_T)^2$ for $\Theta = 60°$	5.49×10^{-2}	11.5	1.00×10^4

NOTE.—We assume the grain properties of Table 4, $\rho = 3$ g cm^{-3}, $\alpha_1 = 1.745$, $\delta = 2$, $n_{\rm H} = 30$ cm^{-3}, $T = 100$ K, $T_d = 18$ K, $f = 1/3$, $n({\rm H})/n_{\rm H} = 1$, $E_{\rm H_2} = 0.2$ eV, $l = 10$ Å, $u_{\rm rad} = u_{\rm ISRF}$, and $\gamma = 0.1$.

Table 5 for three grain sizes and three possible values of the surface recombination site lifetime t_0.

A typical diffuse cloud may have $n_{\rm H}T = 3000$ cm^{-3} K; the average interstellar radiation field then corresponds to $u_{\rm rad}/n_{\rm H}kT = 2.09$. We adopt an anisotropy factor $\gamma = 0.1$ as representative.

As seen from Figures 10 and 11, the spectrum-averaged $\langle \boldsymbol{Q}_\Gamma(\Theta)\rangle \cdot \hat{\boldsymbol{a}}_1$ varies considerably with Θ, the angle between $\hat{\boldsymbol{a}}_1$ and the radiation flux. Values of $(\omega_{\rm rad}/\omega_T)^2$ are given in Table 5 for $\Theta = 0°$ and 60°, and for three grain sizes.

For the $a_{\rm eff} = 0.2$ μm grain at $\Theta = 0°$, we find that radiative torques result in extreme superthermal rotation, with $(\omega_{\rm rad}/\omega_T)^2 \approx 9 \times 10^4$, greater than the rotation due to H_2 formation on the grain surface if $l \lesssim 35$ Å. The $a_{\rm eff} = 0.05$ μm grain, on the other hand, has a radiatively driven rotation rate only slightly in excess of thermal, with $(\omega_{\rm rad}/\omega_T)^2 = 18$ (for $\Theta = 0°$), far smaller than the rotation velocity expected from H_2 formation. The $a_{\rm eff} = 0.02$ μm grain is essentially unaffected by radiative torques: the rotational kinetic energy resulting from these torques is small compared to kT. We therefore see that—at least for the particular shape considered here—radiative torques will drive the larger ($a_{\rm eff} \gtrsim 0.1$ μm) grains to highly superthermal rotation rates, while having only a slight effect on the smaller ($a_{\rm eff} \lesssim 0.05$ μm) grains.

Paramagnetic dissipation can align the grain angular momentum with the magnetic field on the "Davis-Greenstein" timescale

$$\tau_{\rm DG} = \frac{2\alpha_1 \rho a_{\rm eff}^2}{5K(\omega)B_0^2} \tag{68}$$

$$= 1.5 \times 10^6 \alpha_1 \rho_3 a_{-5}^2 \left[\frac{10^{-13}\ {\rm s}}{K(\omega)}\right]\left(\frac{5\ \mu{\rm G}}{B_0}\right)^2 {\rm yr} \tag{69}$$

(Davis & Greenstein 1951), where $K(\omega) \equiv {\rm Im}\,[\chi(\omega)]/\omega \approx 10^{-13}$ s for normal paramagnetism at $T \approx 18$ K (Draine 1996); equation (56) then implies $\tau_{\rm DG} \approx 17 a_{-5}\,\tau_{\rm drag}$.

It has been known for some time that the observed wavelength dependence of polarization requires that if the small grains and large grains have similar shapes, then the degree of alignment declines rapidly for $a_{\rm eff} \lesssim 0.1$ μm (Mathis 1979, 1986; Kim & Martin 1994a, 1994b). This was somewhat unexpected: since $\tau_{\rm DG} \propto a^2$, one might naively expect that small grains would exhibit a *higher* degree of alignment than large grains.

Several ideas have been put forward to explain the low degree of alignment of small grains. Mathis (1986) proposed that a grain would not be aligned unless it contained at least one superparamagnetic inclusion, and that small grains were statistically unlikely to contain such an inclusion. Mathis obtained a good fit to the average polarization curve by assuming that a grain with $a_{\rm eff} = 0.08$ μm had a 50% probability of containing one or more inclusions. Lazarian (1994) argued that if grain alignment was due to the Gold mechanism (gas-grain streaming) driven by Alfvén waves, then only the larger grains ($a_{\rm eff} \gtrsim 0.1$ μm) were sufficiently inertial to be aligned. Lazarian (1995c) argued that H_2 formation on fractal grains would only be able to drive grains with $a_{\rm eff} \gtrsim 0.02$ μm to superthermal rotation.

As pointed out by Purcell (1975, 1979), superthermal rotation contributes to grain alignment by rendering unimportant the disaligning effects of random collisions with gas atoms. Purcell considered three processes that could drive grains to superthermal rotation: H_2 formation on the grain surface, photoelectric emission, and variations in the effective accommodation coefficient over the grain surface; of the three, H_2 formation appears to be the most powerful. As discussed in § 8.1, the effects of this torque depend on the "correlation time" t_0 for the torques driving superthermal rotation. If the only torques are due to H_2 formation and collisions with gas atoms, the grain will undergo spin-down and "crossover events" with a frequency $t_z^{-1} \approx (\pi^2 t_0\,\tau_{\rm drag})^{-1/2}$, with mean time back to the previous crossover $t_b \approx 1.3(t_0 + \tau_{\rm drag})$ (Purcell 1979). Each crossover event will be accompanied by partial disalignment due to random impulses on the grain while it is rotating slowly (Spitzer & McGlynn 1979). If $t_b \ll \tau_{\rm DG}$, then grain alignment by paramagnetic dissipation will be suppressed, whereas if $t_b \gtrsim \tau_{\rm DG}$, then paramagnetic dissipation will result in a high degree of alignment. The three processes discussed by Purcell depend upon surface properties; if the grain surface is altered on a relatively short timescale, then substantial grain alignment will not occur unless the grains are superparamagnetic (in which case $\tau_{\rm DG}$ is short).

Here we propose another mechanism for selective alignment of the larger grains. The radiative torques on the grain depend upon the global geometry of the grain, and will therefore have a correlation time of order the grain lifetime, $\sim 10^8$ yr. For the $a_{\rm eff} = 0.2$ μm grains considered here, $|\Gamma_{\rm rad}|^2 \gg |\Gamma_{\rm H_2}|^2$, and we may expect long-lived superthermal rotation. By itself, long-lived superthermal rotation would lead to grain alignment by paramagnetic dissipation on the Davis-Greenstein timescale $\tau_{\rm DG}$, as expected for "Purcell torques" that are fixed in body coordinates. However, when an anisotropic radiation field is present, the radiative torque components perpendicular to $\hat{\boldsymbol{a}}_1$ may act

TABLE 6

SILICATE GRAINS IN DARK CLOUDS

Parameter	$a_{\rm eff} = 0.02$ μm	$a_{\rm eff} = 0.05$ μm	$a_{\rm eff} = 0.2$ μm
$\tau_{\rm drag,gas}$ (yr)	1.02×10^2	2.56×10^2	1.02×10^3
$\tau_{\rm drag,em}$ (yr)	9.63×10^5	8.29×10^6	2.52×10^8
$\tau_{\rm drag}$ (yr)	1.02×10^2	2.56×10^2	1.02×10^3
ω_T (rad s^{-1})	3.14×10^6	3.17×10^5	9.92×10^3
$(\omega_{\rm H2}/\omega_T)^2$ for $t_0 = 10^4$ yr	0.466	1.15	4.27
$(\omega_{\rm H2}/\omega_T)^2$ for $t_0 \gtrsim 10^5$ yr	0.470	1.17	4.70
$(\omega_{\rm rad}/\omega_T)^2$ for $\Theta = 0°$	1.30×10^{-6}	9.63×10^{-4}	4.04
$(\omega_{\rm rad}/\omega_T)^2$ for $\Theta = 60°$	5.39×10^{-6}	2.10×10^{-4}	0.275

NOTE.—We assume the grain parameters of Table 4, $\rho = 3$ g cm^{-3}, $\alpha_1 = 1.745$, $\delta = 2$, $n_{\rm H} = 10^4$ cm^{-3}, $T = 20$ K, $f = 1/3$, $n({\rm H})/n_{\rm H} = .01$, $E_{\rm H_2} = 0.2$ eV, $l = 10$ Å, $T_d = 10$ K, $u_{\rm rad} = .07 u_{\rm ISRF}$, and $\gamma = 0.7$.

directly to change the grain alignment on timescales short compared to $\tau_{\rm DG}$; it appears that this may be the mechanism responsible for the observed alignment of $a_{\rm eff} \gtrsim 0.1$ μm dust grains with the interstellar magnetic field (Draine & Weingartner 1996).

For the $a_{\rm eff} = 0.05$ μm grains, on the other hand, the radiative torques are weak compared to the Purcell torques due to H_2 formation. If $t_b \ll \tau_{\rm DG}$, there will be frequent crossover events, with a resulting low degree of grain alignment. This may explain the observed preferential alignment of the larger $a_{\rm eff} \gtrsim 0.1$ μm interstellar grains and the minimal alignment of $a_{\rm eff} \lesssim 0.05$ μm grains.

The dynamics of grain alignment, including radiative torques, will be examined in more detail in a later paper (Draine & Weingartner 1996).

8.4. *Dark Clouds*

The alignment of grains in dense clouds has been problematic. Recent studies of polarization of background stars indicate a low degree of grain alignment in the central regions of some dark clouds (Goodman et al. 1995). This has been attributed to lack of superthermal rotation in regions where the hydrogen is predominantly molecular, where the grains are shielded from ultraviolet photons capable of producing photoelectric emission, and where the gas and grain temperatures tend to be similar. However, observations of polarized FIR emission from M17, M42 (Orion), and W3 (Hildebrand et al. 1995; Hildebrand 1996) shows that the grains responsible for the FIR emission in these dark clouds are significantly aligned, and it has not been clear why grains in some dense molecular regions are aligned, while in others they are not.

The dark cloud L1755 observed by Goodman et al. (1995) has $n_{\rm H} \approx 10^4$ cm^{-3} and $T \approx 20$K, with a peak extinction through the cloud $A_V \gtrsim 8$. We suppose the cloud to be externally illuminated by the average interstellar radiation field. At the cloud surface, we have $u_{\rm rad} \approx 0.5 u_{\rm ISRF}$ and $\gamma = 0.5$, and at a depth $A \approx 2$ mag from the cloud surface, we estimate[6] $u_{\rm rad} \approx 0.07 u_{\rm ISRF}$, $\gamma \approx 0.7$; the radiation will of course be substantially reddened, but we neglect this here. Table 6 lists values of $(\omega_{\rm rad}/\omega_T)^2$ for grains at this depth. We see that the weakened radiation field, and the higher gas density, make the radiative torques relatively unimportant in this environment. Near the cloud surface, of course, conditions are closer to the diffuse cloud conditions of Table 5, and radiative torques will maintain superthermal rotation. Thus, we expect grain alignment near the cloud surface, but not at depths $A \gtrsim 2$ mag.

8.5. *Star-Forming Clouds*

In star-forming clouds, there are obviously sources of starlight within the clouds. To estimate the characteristic starlight energy density to which the FIR-emitting dust is exposed, we note that for grains with far-infrared emissivity $Q_{\rm abs} \propto \lambda^{-2}$, the power radiated by the grain $P \propto T_d^6$, where T_d is the grain temperature. If we assume that the grain is heated by starlight with an energy density $u_{\rm rad}$, then, since the average interstellar radiation field $u_{\rm ISRF}$ heats grains to $T_d \approx 18$ K, we find

$$u_{\rm rad} \approx \left(\frac{T_d}{18\ {\rm K}}\right)^6 u_{\rm ISRF} \,. \tag{70}$$

As an example, we consider one point on the M17 molecular cloud: $(\alpha, \delta) = (18^{\rm h}17^{\rm m}40^{\rm s}, -15°16')$. The 100 μm emission at this point has a linear polarization of ~5% (Hildebrand et al. 1995), indicating that the grains are

[6] If the dust has albedo ~0.5 and is highly forward-scattering, then $u_{\rm rad} \approx 0.5 u_{\rm rad} E_2(0.5A/1.086)$, $\gamma \approx E_3(0.5A/1.086)/E_2(0.5A/1.086)$, where E_2 and E_3 are exponential integrals. For $A = 2$, we would have $u_{\rm rad} \approx .0742 u_{\rm ISRF}$, $\gamma \approx 0.739$.

TABLE 7

SILICATE GRAINS IN STAR-FORMING CLOUDS

Parameter	$a_{\rm eff} = 0.02$ μm	$a_{\rm eff} = 0.05$ μm	$a_{\rm eff} = 0.2$ μm
$\tau_{\rm drag,gas}$ (yr)	6.82	17.1	68.2
$\tau_{\rm drag,em}$ (yr)	812.0	6.99×10^3	2.13×10^5
$\tau_{\rm drag}$ (yr)	6.76	17.1	68.2
ω_T (rad s^{-1})	4.70×10^6	4.76×10^5	1.49×10^4
$(\omega_{\rm H2}/\omega_T)^2$ for $t_0 \gtrsim 10^4$ yr	0.209	0.522	2.09
$(\omega_{\rm rad}/\omega_T)^2$ for $\Theta = 0°$	7.59×10^{-3}	2.65	1.79×10^4
$(\omega_{\rm rad}/\omega_T)^2$ for $\Theta = 60°$	1.42×10^{-2}	1.31	1.38×10^3

NOTE.—We assume the grain parameters of Table 4, $\rho = 3$ g cm^{-3}, $\alpha_1 = 1.745$, $\delta = 2$, $n_{\rm H} = 10^5$ cm^{-3}, $T = 45$ K, $f = 1/3$, $n({\rm H})/n_{\rm H} = .01$, $E_{\rm H_2} = 0.2$ eV, $l = 10$ Å, $T_d = 45$ K, $u_{\rm rad} = 240 u_{\rm ISRF}$, and $\gamma = 0.3$.

appreciably aligned. The emission from the dust has a 50 μm/100 μm color temperature of $\sim$85 K (Gatley et al. 1979); for a λ^{-2} emissivity, this color temperature corresponds to a dust temperature $T_d \approx 45$ K. If heated radiatively, these grains must therefore be exposed to a radiation field[7] with $u_{\rm rad}/u_{\rm ISRF} \approx (45/18)^6 = 240$ if the radiation heating the grains has a spectrum similar to interstellar starlight (ISRF). While the spectrum no doubt differs from the ISRF spectrum, it is not obvious how: the embedded massive stars will tend to be bluer, but the spectrum will be reddened by propagation through the dust. For the present purposes, we will assume the ISRF spectrum, with an anisotropy factor $\gamma = 0.3$. The gas in M17 has $n_{\rm H} \approx 10^5$ cm^{-3} (see Stutzki & Güsten 1990), and presumably has $T \approx 45$ K, close to the grain temperature. We use equation (67) to obtain the $\omega_{\rm rad}$ values given in Table 7. We see that $a_{\rm eff} = 0.2$ μm grains will have $(\omega_{\rm rad}/\omega_T)^2 \approx 2 \times 10^4$ (for $\Theta = 0°$). Evidently, the radiation field within a star-forming region like M17 is sufficiently intense to drive extreme superthermal rotation of the $a_{\rm eff} \gtrsim 0.1$ μm grains. In addition to producing superthermal rotation, the components of the radiative torques perpendicular to $\hat{\boldsymbol{a}}_1$ may bring about the observed grain alignment (Draine & Weingartner 1996).

9. SUMMARY

The principal results in this paper are as follows:

1. We show how forces and torques on an irregular grain may be calculated using the discrete dipole approximation.

2. We report numerical results (in Fig. 6 and Table 4) for $\hat{\boldsymbol{k}} \cdot \boldsymbol{Q}_{\rm pr}(\lambda)$, the component of the radiation pressure efficiency vector parallel to the radiative flux for one particular irregular grain geometry, where the grain is assumed to be spinning around its principal axis $\hat{\boldsymbol{a}}_1$ of largest moment of inertia.

3. We report numerical results for the "radiation torque efficiency vector" $\boldsymbol{Q}_\Gamma(\lambda)$, (in Figs. 8–15) for one irregular grain geometry. The torque depends upon the angle Θ between the incident flux and the grain rotation axis $\hat{\boldsymbol{a}}_1$.

4. In interstellar diffuse clouds, radiative torques will drive $a_{\rm eff} \gtrsim 0.1$ μm grains to extreme superthermal rotation.

5. Radiative torques will dominate the torques due to H_2 formation for $a_{\rm eff} \gtrsim 0.1$ μm interstellar grains. For these grains, the superthermal rotation is expected to be very long-lived, since it depends upon global properties of the grain, rather than the relatively short-lived surface properties that determine superthermal rotation due to H_2 formation, photoelectric emission, or variations in surface accommodation coefficient.

6. In an isotropic radiation field, the long-lived superthermal rotation of $a_{\rm eff} \gtrsim 0.1$ μm grains due to radiative torques would facilitate alignment of these grains with the Galactic magnetic field by the Davis-Greenstein mechanism of paramagnetic relaxation.

7. Since the rotation of smaller ($a \lesssim 0.05$ μm) grains is not dominated by radiative torques, alignment of these grains with the Galactic magnetic field would be limited as a result of random variations in the torque associated with H_2 formation on the grain surface. This may explain why $a_{\rm eff} \gtrsim 0.1$ μm grains in diffuse clouds are aligned, while there is evidently minimal alignment of the $a_{\rm eff} \lesssim 0.05$ μm grains, which dominate the extreme ultraviolet extinction.

8. Radiative torques appear to be able to drive grains to superthermal rotation in star-forming regions, such as M17, where the ratio of anisotropic radiation to gas pressure is relatively high, thereby potentially explaining the observed alignment of far-infrared–emitting dust in M17 and other star-forming regions with warm dust. In cold dark clouds, on the other hand, radiative torques are unable to drive the grains to superthermal rotation, consistent with the observed lack of aligned grains deep in quiescent dark clouds.

9. In addition to the torque component parallel to the grain rotation axis $\hat{\boldsymbol{a}}_1$ (which drives superthermal rotation), anisotropy of the radiation field can result in radiative torque components perpendicular to the grain angular momentum; these components can affect grain alignment directly.

This research was supported in part by NSF grant AST-9219283 to B. T. D., and by an NSF Graduate Research Fellowship to J. C. W. We are grateful to R. H. Lupton for the availability of the SM plotting package and to A. Lazarian, W. G. Roberge, and L. Spitzer for helpful comments.

[7] For $T_d = 45$ K, the 50 μm optical depth at this position is $\tau(50\ \mu{\rm m}) \approx 0.08$, so that the grains must be heated by radiation at $\lambda \ll 50$ μm.

APPENDIX A

RADIATION FIELD DUE TO OSCILLATING DIPOLES

Consider an array of oscillating point electric dipoles $\boldsymbol{p}_j$, at locations $\boldsymbol{r}_j$. At large distances r, the fields due to these dipoles may be written

$$\boldsymbol{E}_{\rm sca} = e^{ikr} \sum_{j=1}^{N} \left(\frac{k^2}{r} [\boldsymbol{p}_j - \hat{\boldsymbol{n}}(\hat{\boldsymbol{n}} \cdot \boldsymbol{p}_j)] + \boldsymbol{p}_j \frac{k^2}{r^2} \left\{ (\hat{\boldsymbol{n}} \cdot \boldsymbol{r}_j) + \frac{ik[r_j^2 - (\hat{\boldsymbol{n}} \cdot \boldsymbol{r}_j)^2]}{2} + \frac{i}{k} \right\} \right.$$
$$\left. + \hat{\boldsymbol{n}} \frac{k^2}{r^2} \left[(\boldsymbol{r}_j \cdot \boldsymbol{p}_j) - (\hat{\boldsymbol{n}} \cdot \boldsymbol{p}_j) \left\{ 3(\hat{\boldsymbol{n}} \cdot \boldsymbol{r}_j) + \frac{3i}{k} + \frac{ik}{2} [r_j^2 - (\hat{\boldsymbol{n}} \cdot \boldsymbol{r}_j)^2] \right\} \right] + \boldsymbol{r}_j \frac{k^2}{r^2} (\hat{\boldsymbol{n}} \cdot \boldsymbol{p}_j) \right) \exp(-ik\hat{\boldsymbol{n}} \cdot \boldsymbol{r}_j) + O(r^{-3}), \quad \text{(A1)}$$

$$\boldsymbol{B}_{\rm sca} = e^{ikr} \sum_{j=1}^{N} \left[\frac{k^2}{r} \hat{\boldsymbol{n}} \times \boldsymbol{p}_j + \frac{k^2}{r^2} \left\{ 2(\hat{\boldsymbol{n}} \cdot \boldsymbol{r}_j) + \frac{ik}{2} [r_j^2 - (\hat{\boldsymbol{n}} \cdot \boldsymbol{r}_j)^2] - \frac{1}{ik} \right\} \hat{\boldsymbol{n}} \times \boldsymbol{p}_j - \frac{k^2}{r^2} \boldsymbol{r}_j \times \boldsymbol{p}_j \right] \exp(-ik\hat{\boldsymbol{n}} \cdot \boldsymbol{r}_j) + O(r^{-3}). \quad \text{(A2)}$$

Thus,

$$\hat{\boldsymbol{n}} \cdot \boldsymbol{E}_{\rm sca} = \frac{k^2}{r^2} e^{ikr} \sum_{j=1}^{N} \left\{ (\boldsymbol{r}_j \cdot \boldsymbol{p}_j) - (\hat{\boldsymbol{n}} \cdot \boldsymbol{p}_j) \left[(\hat{\boldsymbol{n}} \cdot \boldsymbol{r}_j) + \frac{2i}{k} \right] \right\} \exp\left(-ik\hat{\boldsymbol{n}} \cdot \boldsymbol{r}_j\right) + O(r^{-3}) , \tag{A3}$$

$$\boldsymbol{E}_{\rm sca} \times \hat{\boldsymbol{n}} = \frac{k^2}{r} e^{ikr} \sum_{j=1}^{N} \boldsymbol{p}_j \times \hat{\boldsymbol{n}} \exp\left(-ik\hat{\boldsymbol{n}} \cdot \boldsymbol{r}_j\right) + O(r^{-2}) , \tag{A4}$$

$$\hat{\boldsymbol{n}} \cdot \boldsymbol{B}_{\rm sca} = \frac{k^2}{r^2} e^{ikr} \hat{\boldsymbol{n}} \cdot \sum_{j=1}^{N} \boldsymbol{p}_j \times \boldsymbol{r}_j \exp\left(-ik\hat{\boldsymbol{n}} \cdot \boldsymbol{r}_j\right) + O(r^{-3}) , \tag{A5}$$

$$\boldsymbol{B}_{\rm sca} \times \hat{\boldsymbol{n}} = \frac{k^2}{r} e^{ikr} \sum_{j=1}^{N} [\boldsymbol{p}_j - \hat{\boldsymbol{n}}(\hat{\boldsymbol{n}} \cdot \boldsymbol{p}_j)] \exp\left(-ik\hat{\boldsymbol{n}} \cdot \boldsymbol{r}_j\right) + O(r^{-2}) . \tag{A6}$$

These expressions, substituted into equation (26), lead to the result (27) for the time-averaged torque $\langle \boldsymbol{\Gamma}_{\rm out} \rangle$.

REFERENCES

Bohren, C. F., & Huffman, D. R. 1983, Absorption and Scattering of Light by Small Particles (New York: Wiley)
Davis, L., & Greenstein, J. L. 1951, ApJ, 114, 206
Dolginov, A. Z. 1972, Ap&SS, 18, 337
Dolginov, A. Z., & Mytrophanov, I. G. 1976, 43, 291
Dolginov, A. Z., & Silant'ev, N. A. 1976, Ap&SS, 43, 337
Draine, B. T. 1988, ApJ, 333, 848
———. 1994, in ASP Conf. Ser. 58, First Symp. Infrared Cirrus and Diffuse Interstellar Clouds, ed. R. M. Cutri & W. B. Latter (San Francisco: ASP), 227
———. 1996, in ASP Conf. Ser. 97, Polarimetry of the Interstellar Medium, ed. W. G. Roberge & D. C. B. Whittet (San Francisco: ASP), 16
Draine, B. T., & Flatau, P. J. 1994, J. Opt. Soc. Am. A, 11, 1491
Draine, B. T., & Goodman, J. 1993, ApJ, 405, 685
Draine, B. T., & Lee, H. M. 1984, ApJ, 285, 89
Draine, B. T., & Weingartner, J. C. 1996, in preparation
Duley, W. W. 1978, ApJ, 219, L129
Flatau, P. J. 1996, in preparation
Gatley, I., Becklin, E. E., Sellgren, K., & Werner, M. W. 1979, ApJ, 233, 575
Gold, T. 1952, MNRAS, 112, 215
Goodman, A. A., Jones, T. J., Lada, E. A., & Myers, P. C. 1995, ApJ, 448, 748
Goodman, A. A., & Whittet, D. C. B. 1995, ApJ, 455, L181
Goodman, J., Draine, B. T., & Flatau, P. J. 1991, Opt. Lett., 16, 1198
Hall, J. S. 1949, Science, 109, 166
Hall, J. S., & Mikesell, A. H. 1949, AJ, 54, 187
Harwit, M. 1970a, Nature, 226, 61
———. 1970b, Bull. Astron. Inst. Czechoslovakia, 21, 204
Hildebrand, R. H. 1996, in ASP Conf. Ser. 97, Polarimetry of the Interstellar Medium, ed. W. G. Roberge & D. C. B. Whittet (San Francisco: ASP), 254
Hildebrand, R. H., Dotson, J. L., Dowell, C. D., Platt, S. R., Schleuning, D., Davidson, J. A., & Novak, G. 1995, in ASP Conf. Ser. 73, Airborne Astronomy Symposium on the Galactic Ecosystem, ed. M. R. Haas, J. A. Davidson, & E. F. Erickson (San Francisco: ASP), 97
Hiltner, W. A. 1949a, Science, 109, 165
———. 1949b, ApJ, 109, 471
Jackson, J. D. 1975, Classical Electrodynamics (New York: Wiley)
Jones, R. V., & Spitzer, L. 1967, ApJ, 147, 943
Kim, S.-H., & Martin, P. G. 1994a, ApJ, 431, 783
———. 1994b, ApJ, 444, 293
Lazarian, A. 1994, MNRAS, 268, 713
———. 1995a, ApJ, 451, 660
———. 1995b, MNRAS, 277, 1235
———. 1995c, A&A, 293, 859
Martin, P. G. 1995, ApJ, 445, L63
Mathis, J. S. 1979, ApJ, 232, 747
———. 1986, ApJ, 308, 281
Mathis, J. S., Mezger, P. G., & Panagia, N. 1983, A&A, 128, 212
Mezger, P. G., Mathis, J. S., & Panagia, N. 1982, A&A, 105, 372
Purcell, E. M. 1975, in The Dusty Universe, ed. G. B. Field & A. G. W. Cameron (New York: Neal Watson), 155
———. 1979, ApJ, 231, 404
Purcell, E. M., & Spitzer, L. 1971, ApJ, 167, 31
Roberge, W. G., deGraff, T. A., & Flaherty, J. E. 1993, ApJ, 418, 287
Roberge, W. G., Hanany, S., & Messinger, D. W. 1995, ApJ, 453, 238
Spitzer, L., & McGlynn, T. A. 1979, ApJ, 231, 417
Stutzki, J., & Güsten, R. 1990, ApJ, 356, 513